

# Accreting Black Holes

Cosimo Bambi and Sourabh Nampalliwar

**Abstract** This chapter provides a general overview on the main astronomical observations of black holes in the Universe and on their interpretation. We briefly review the spectral state classification, the AGN classification, and the leading techniques for measuring black hole spins (continuum-fitting method and X-ray reflection spectroscopy). We also introduce quasi-periodic oscillations, the possible detection of the shadow of black holes, and the observations and the theoretical models of jets.

## 1 Black hole classes

Any astrophysical black hole should be completely characterized by its mass  $M$  and its spin parameter  $a_*$ . The spin parameter cannot be arbitrary and must satisfy the constraint  $|a_*| \leq 1$ , which is the condition for the existence of the event horizon, as shown in the previous chapter. On the contrary, there are no theoretical constraints on the value of the mass of a black hole, which may thus be arbitrarily small as well as arbitrarily large.

From astronomical observations, we have strong evidence of two classes of astrophysical black holes:

1. *Stellar-mass black holes* [121].
2. *Supermassive black holes* [71].

There is also some evidence of *intermediate-mass black holes*, with a mass filling the gap between the stellar-mass and the supermassive ones [28].

---

Cosimo Bambi (✉)

Department of Physics, Fudan University, 2005 Songhu Road, Shanghai 200438, China, e-mail: bambi@fudan.edu.cn

Sourabh Nampalliwar

Theoretical Astrophysics, Eberhard-Karls Universität Tübingen, Auf der Morgenstelle 10, 72076 Tübingen, Germany, e-mail: sourabh.nampalliwar@uni-tuebingen.de

Black holes should form from the complete gravitational collapse of a system, when there is no mechanics capable of balancing the gravitational force and the system shrinks until the formation of the event horizon. The collapse of the core of heavy stars is expected to produce black holes with a mass  $M \gtrsim 3 M_{\odot}$  because for cores of lower mass the quantum pressure of neutrons should stop the collapse and the final product should be a neutron star [123, 64, 75]. There are cosmological scenarios in which it is possible to produce *primordial black holes* with any mass, even much lower than  $3 M_{\odot}$  [69]. Nevertheless, for the moment there is no evidence for the existence of such objects.

Note that in the X-ray and  $\gamma$ -ray communities it is common to use the term *black hole binary* or *Galactic black hole* to indicate a stellar-mass black hole in an X-ray binary system, and the term *AGN* (active galactic nucleus) to mean a supermassive black hole in an AGN.

### 1.1 Stellar-mass black holes

From stellar evolution simulations, we expect that in our Galaxy there is a population of  $10^8$ - $10^9$  black holes formed at the end of the evolution of heavy stars [151, 148], and the same number can be expected in similar galaxies. The initial mass of a stellar-mass black hole should depend on the properties of the progenitor star: on its mass, its evolution, and the supernova explosion mechanism [14]. A crucial quantity is the metallicity of the star, namely the fraction of mass of the star made of elements heavier than helium.

The maximum mass of black hole remnants critically depends on the metallicity. The final mass of the remnant is indeed determined by the mass loss rate by stellar winds, which increases with the metallicity because heavier elements have a larger cross section than lighter ones, and therefore they evaporate faster. For a low-metallicity star [59, 58, 132], there may be a mass gap in the remnant, roughly between 50 and  $150 M_{\odot}$ , namely the mass of the black hole remnant can be  $M \lesssim 50 M_{\odot}$  or  $M \gtrsim 150 M_{\odot}$ . As the metallicity increases, black holes with  $M \gtrsim 150 M_{\odot}$  disappear, mainly because of the increased mass loss rate. Note, however, that some models do not find remnants with a mass above the gap, because stars with  $M \gtrsim 150 M_{\odot}$  may undergo a runaway thermonuclear explosion that completely destroys the system, without leaving any black hole remnant [59, 58].

The lower bound may come from the maximum mass for a neutron star: the exact value is currently unknown, because it depends on the equation of state of matter at super-nuclear densities, but it should be around  $2$ - $3 M_{\odot}$ . For bodies with a mass lower than this limit, the quantum neutron pressure can stop the collapse and the final product is a neutron star. For bodies exceeding this limit, the final product is a black hole [123, 64, 75]. Note, however, that there may be a mass gap between the maximum neutron star mass and the minimum black hole mass [35].

Stellar-mass black holes may thus have a mass in the range  $3$ - $100 M_{\odot}$ . At the moment, all the known stellar-mass black holes in X-ray binaries have a mass  $M \approx 3$ -

$20 M_{\odot}$  [24]. Gravitational waves have shown the existence of heavier stellar-mass black holes. In particular, the event called GW150914 was associated to the coalescence of two black holes with a mass  $M \approx 30 M_{\odot}$  that merged to form a black hole with  $M \approx 60 M_{\odot}$  [1].

While we expect a huge number of stellar-mass black holes in the Galaxy, we only know about 20 objects with a dynamical measurement of the mass and about 50 objects without a dynamical measurement of their mass (it is thus possible that some of them are not black holes but neutron stars). This is because their detection is very challenging. The simplest case is when the black hole is in a binary system and has a companion star. The presence of a compact object can be discovered from the observation of a short timescale variability, the non-detection of a stellar spectrum, etc. If we can study the orbital motion of the companion star, we may be able to measure the mass function [24]

$$f(M) = \frac{K_c^3 P_{\text{orb}}}{2\pi G_{\text{N}}} = \frac{M \sin^3 i}{(1+q)^2}, \quad (1)$$

where  $K_c = v_c \sin i$ ,  $v_c$  is the velocity of the companion star,  $i$  is the angle between the normal of the orbital plane and our line of sight,  $P_{\text{orb}}$  is the orbital period of the system,  $q = M_c/M$ ,  $M_c$  is the mass of the companion, and  $M$  is the mass of the dark object. If we can somehow estimate  $i$  and  $M_c$ , we can infer  $M$ , and in this case we talk about dynamical measurement of the mass. The dark object is a black hole if  $M > 3 M_{\odot}$  [123, 64, 75].

Note that, among astronomers, it is common to call “black hole” a stellar-mass compact object that is supposed to be a black hole and for which there is a dynamical measurement of its mass proving that  $M > 3 M_{\odot}$ . The latter indeed guarantees that the object is too heavy for being a neutron star. “Black hole candidates” are instead stellar-mass compact objects that are supposed to be black holes, for instance because of the detection of spectral features typical of black holes, but for which there is no dynamical measurement of their mass.

Black holes in X-ray binaries (black hole binaries<sup>1</sup>) are grouped into two classes: *low-mass X-ray binaries* (LMXBs) and *high-mass X-ray binaries* (HMXBs). “Low” and “high” is referred to the stellar companion, not to the black hole: in the case of LMXBs, the companion star has normally a mass  $M_c < 3 M_{\odot}$ , while for HMXBs the companion star has  $M_c > 10 M_{\odot}$ . Observationally, we can classify black hole binaries either as *transient X-ray sources* or *persistent X-ray sources*. LMXBs are usually transient sources, because the mass transfer is not continuous (for instance, at some point the surface of the companion star may expand and the black hole strips some gas): the system may be bright for a period ranging from some days to a few months and then be in a quiescent state for months or even decades. We expect  $10^3$ -

---

<sup>1</sup> Generally speaking, a *black hole binary* is a binary system in which at least one of the two bodies is a black hole, and a *binary black hole* is a binary system of two black holes. In the context of stellar-mass black holes, the term black hole binary is used to indicate a binary system of a black hole with a stellar companion. In the context of supermassive black holes, it is common to call black hole binary a system of two supermassive black holes.

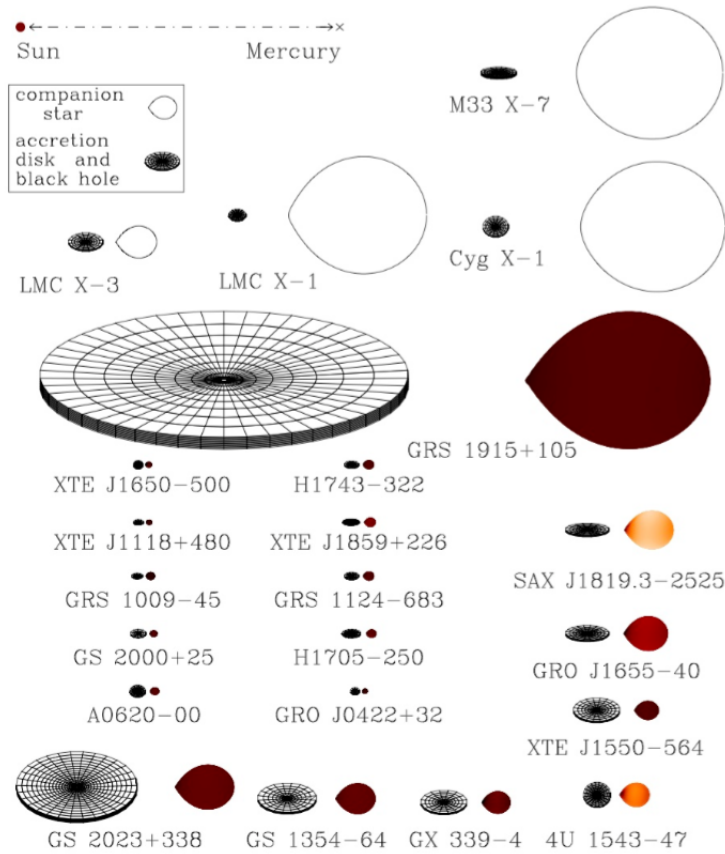


Fig. 1: Sketch of 22 X-ray binaries with a stellar-mass black hole confirmed by dynamical measurements. For every system, the black hole accretion disk is on the left and the companion star is on the right. The color of the companion star roughly indicates its surface temperature (from brown to white as the temperature increases). The orientation of the disks indicates the inclination angles of the binaries. For comparison, in the top left corner of the figure we see the system Sun-Mercury: the distance between the two bodies is about 50 millions km and the radius of the Sun is about 0.7 millions km. Figure courtesy of Jerome Orosz.

$10^4$  LMXBs in the Galaxy [168, 65] and every year we discover 1-2 new objects, when they pass from their quiescent state to an outburst (see Section 3). HMXBs are persistent sources: the mass transfer from the companion star to the black hole is a relatively regular process (typically it is due to the stellar wind of the companion) and the binary is a bright source at any time without quiescent periods.

Fig. 1 shows 22 X-ray binaries with a stellar-mass black hole confirmed by dynamical measurements. To have an idea of the size of these systems, the figure also shows the Sun (whose radius is 0.7 millions km) and the distance Sun-Mercury (about 50 millions km). The black holes have a radius  $< 100$  km and cannot be seen, but we can clearly see their accretion disks formed from the transfer of material from the companion star. The latter may have a quite deformed shape (in particular, we can see some cusps) due to the tidal force produced by the gravitational field of the black hole. In Fig. 1, Cygnus X-1 (Cyg X-1 in Fig. 1), LMC X-1, LMC X-3, and M33 X-7 are HMXBs, while all other systems are LMXBs. Among these HMXBs, only Cygnus X-1 is in our Galaxy. Among the LMXBs, there is GRS 1915+105, which is quite a peculiar source: since 1992, it is a bright X-ray source in the sky, so it can be considered a persistent source. This is probably because of its large accretion disk, which can provide enough material at any time.

Black holes in compact binary systems (black hole-black hole or black hole-neutron star) can be detected with gravitational waves when the signal is sufficiently strong, which means just before merger. Fig. 2 shows the first detections by the LIGO/Virgo collaboration. The name of the event is classified as GW (gravitational wave event) and then there is the date: for example, GW150914 was detected on 14 September 2015. LVT151012 is not classified as a gravitational wave event because it may have been caused by noise<sup>2</sup>. For every event, the figure shows the two original black holes as well as the final one after merger.

Isolated black holes are much more elusive. In principle, they can be detected by observing the modulation of the light of background stars due to the gravitational lensing caused by the passage of a black hole along the line of sight of the observer [8].

## 1.2 Supermassive black holes

Astronomical observations show that at the center of many galaxies there is a large amount of mass in a relatively small volume. The standard interpretation is that these objects are supermassive black holes with  $M \sim 10^5$ - $10^{10} M_{\odot}$ . The strongest constraints come from the center of the Galaxy and NGC 4258. For the Galaxy, we can study the Newtonian motion of individual stars and infer that at the center there is an object with a mass of  $4 \cdot 10^6 M_{\odot}$  (see Fig. 3). An upper bound on the size of this body can be obtained from the minimum distance approached by one of these stars, which is less than 45 AU and corresponds to  $\sim 1,200 r_g$  for a  $4 \cdot 10^6 M_{\odot}$  object. In the end, we can exclude the existence of a cluster of compact non-luminous bodies like neutron stars and therefore we can conclude that the most natural interpretation is that it is a supermassive black hole [81]. In the case of NGC 4258, we can study the orbital motion of gas in the nucleus, and again we can conclude that the central object is too massive, compact, and old to be a cluster of neutron

---

<sup>2</sup> LVT stands for LIGO/Virgo transient.

stars [81]. In the case of other galaxies, it is not possible to put such constraints with the available data, but it is thought that every middle-size (like the Galaxy) or large galaxy has a supermassive black hole at its center<sup>3</sup>. For lighter galaxies, the situation is more uncertain. Most models predict supermassive black holes at the center of lighter galaxies as well [154], but there are also models predicting the existence of a population of faint low-mass galaxies with no supermassive black hole at their center [156, 155]. Observations suggest that some small galaxies have a supermassive black hole and other small galaxies do not [38, 43].

In the case of stellar-mass black holes, it is easy to argue that they are the final product of the evolution of very heavy stars. In the case of supermassive black holes, at the moment we do not know their exact origin. We just observe supermassive objects in galactic nuclei with masses  $M \sim 10^5$ - $10^{10} M_{\odot}$ . More puzzlingly, we observe objects with masses  $M \sim 10^{10} M_{\odot}$  even in very distant galaxies [164], when the Universe was only 1 billion years old, and we do not know how such objects were created and were able to grow so fast in a relatively short time [154]. The Eddington accretion rate can be exceeded in some accretion models, and this may indeed be a possible path to the rapid growth of supermassive black holes [80]. The possibility of super-Eddington accretion is confirmed, for instance, by the observation of a neutron star in the galaxy M82 with a luminosity exceeding its Eddington limit [9]. It is also possible that supermassive black holes formed from the collapse of heavy

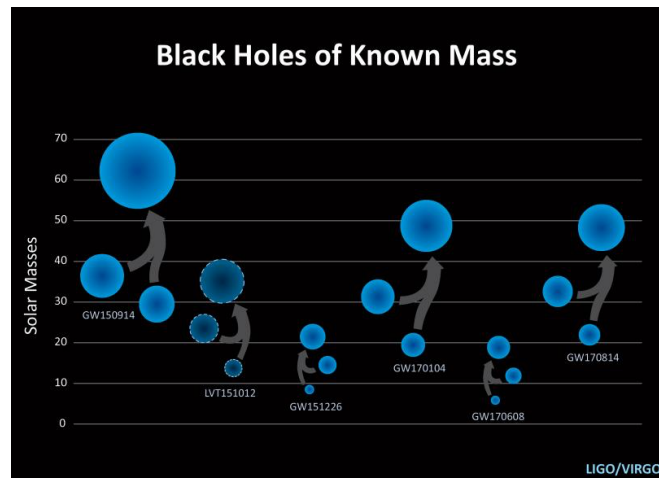


Fig. 2: Masses of the first black holes observed with gravitational waves, with the two initial objects merging into a larger one, as shown by the arrows. Image Credit: LIGO/NSF/Caltech/SSU Aurore Simmonet.

<sup>3</sup> Exceptions may be possible: the galaxy A2261-BCG has a very large mass but it might not have any supermassive black hole at its center [114].

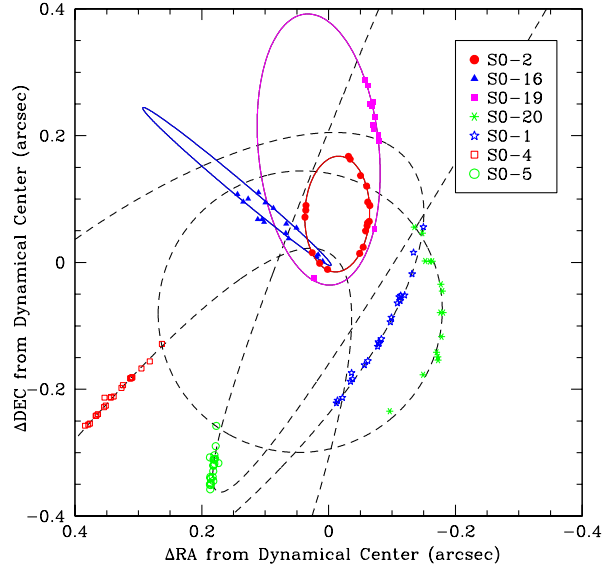


Fig. 3: Astrometric positions and orbital fits for seven stars orbiting the supermassive black hole at the center of the Galaxy. From [49]. ©AAS. Reproduced with permission.

primordial clouds rather than of stars, or that they formed from the merger of several black holes [154].

### 1.3 Intermediate mass black holes

Intermediate-mass black holes are, by definition, black holes with a mass between the stellar-mass and the supermassive ones, say  $M \sim 10^2\text{-}10^5 M_\odot$ . At the moment, there is no dynamical measurement of the mass of these objects, and their actual nature is still controversial.

Some intermediate-mass black hole candidates are associated to ultra luminous X-ray sources [27]. These objects have an X-ray luminosity  $L_X > 10^{39}$  erg/s, which exceeds the Eddington luminosity of a stellar-mass object, and they may thus have a mass in the range  $10^2\text{-}10^5 M_\odot$ . However, we cannot exclude they are actually stellar-mass black holes (or neutron stars [9]) with non-isotropic emission and a moderate super-Eddington mass accretion rate [105].

The existence of intermediate-mass black holes is also suggested by the detection of some quasi-periodic oscillations (QPOs, see Section 6.3) in some ultra-luminous

X-ray sources. QPOs are currently not well understood, but they are thought to be associated to the fundamental frequencies of the oscillation of a particle around a black hole. Since the size of the system scales as the black hole mass, QPOs should scale as  $1/M$ , and some observations may indicate the existence of compact objects with masses in the range  $10^2$ - $10^5 M_\odot$  [110].

Intermediate-mass black holes may be expected to form at the center of dense stellar clusters by merger. Several studies have tried to explore the possible existence of these objects from the observations of the motion of the stars in certain clusters. The presence of an intermediate-mass black hole at the center of the cluster should increase the velocity dispersion in the cluster. Some studies suggest that there are indeed intermediate-mass black holes at the center of certain globular clusters [47, 48], but there is not yet a common consensus.

## 2 Accretion models

Accretion onto a black hole is possible because the gravitational field of the compact object pulls material from the host environment towards the black hole. Some mechanism must remove the angular momentum of this material to cause matter to spiral down into the black hole. The gravitational energy of the material is converted into heat and kinetic energy of the accreting matter, and a part is radiated away. For a review on the theory of black hole accretion models, see for instance [4].

The morphology of the accretion flow is mainly determined by two factors: *i*) the angular momentum of the accreting gas, and *ii*) the mass accretion rate. Depending on the value of these two quantities, we have different accretion processes and different electromagnetic spectra for the accretion flow. Tab. 1 summarizes the main accretion scenarios according to the specific angular momentum of the accreting gas  $L$  (in units of  $r_g c$ ) and the mass accretion rate  $\dot{M}$  (in Eddington units).

In the case of spherically symmetric accretion (vanishing or negligible angular momentum of the accreting gas), we have the so-called *Bondi accretion*, which essentially describes particles in free fall and the radiative efficiency is very low [19, 129], i.e. the gravitational energy of the falling particles is mainly converted into their kinetic energy and lost into the black hole after crossing the event horizon.

However, in typical accretion flows around black holes the gas has a non-negligible angular momentum, and in such a case we have the creation of a disk (see Fig. 4). For stellar-mass black holes with a companion star, the disk is created by the mass transfer from the stellar companion to the black hole. In the case of supermassive black holes in galactic nuclei, the disk forms from the material in the interstellar medium [130] or as a result of galaxy merger [13, 85].

An accretion disk is *geometrically thin (thick)* if  $h/r \ll 1$  ( $h/r \sim 1$ ), where  $h$  is the semi-thickness of the disk at the radial coordinate  $r$ . The disk is *optically thin (thick)* if  $h \ll \lambda$  ( $h \gg \lambda$ ), where  $\lambda$  is the photon mean free path in the medium of the disk. If the disk is optically thick, we see the radiation emitted from the surface of the disk, like in the case of stars.



$Lc/G_N M$	$\dot{M}/\dot{M}_{\text{Edd}}$	Accretion Model	$h/r$	$h/\lambda$	$\eta_r$
$\ll 1$	Any	Bondi Accretion	–	Any	$\ll 0.1$
$> 1$	$> 1$	Thick Disk	$\sim 1$	$\gg 1$	$\ll 0.1$
$> 1$	$0.3 - 1$	Slim Disk	$< 1$	$\gg 1$	$< 0.1$
$> 1$	$0.05 - 0.3$	Thin Disk	$\ll 1$	$\gg 1$	$\sim 0.1$
$\lesssim 1$	$\ll 1$	ADAF	$\sim 1$	$\ll 1$	$\ll 0.1$

Table 1: Summary of the main scenarios of accretion processes around black holes and of their basic properties. The first column indicates the angular momentum of the accreting gas; the second column is for the mass accretion rate (in Eddington units); the third column indicates the name of the accretion model; the fourth column indicates if the accretion disk is geometrically thick or thin; the fifth column shows if the accretion flow is optically thick or thin; the last column is for the radiative efficiency. See the text for more details.

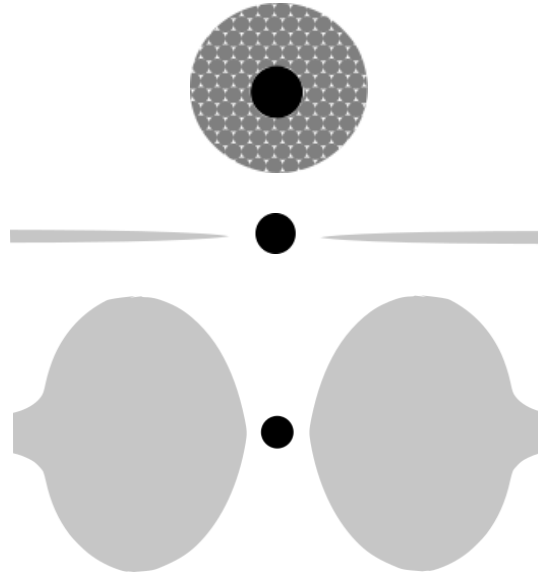


Fig. 4: Sketch of Bondi accretion (top), thin disk (middle), and thick disk (bottom). The black hole is indicated by the black filled circle and the accretion flow is represented by the gray shape.

There are four main types of accretion disk structures, according to the mass accretion rate:

- *Thick disk* [63, 2]. If the mass accretion rate is super-Eddington, the gas pressure makes the disk inflate. The disk is thus geometrically thick. Since the particle density is high, the disk is optically thick and it cannot efficiently radiate away energy from its surface.
- *Slim disk* [3]. As the mass accretion rate decreases, the thickness of the disk decreases too. A slim disk describes the situation between a thick and a thin disk.
- *Thin disk* [128]. For moderate accretion rates, the gas pressure is negligible and we have a geometrically thin and optically thick disk. The radiative efficiency is high because the disk surface is large enough with respect to the mass accretion rate to radiate away the gravitational energy converted into heat. The standard model for thin disks around black holes is the Novikov-Thorne model [104, 106], which is briefly described in Section 2.1.
- *Advection-dominated accretion flow (ADAF)* [100, 101]. If the mass accretion rate is very low, the disk evaporates and we have a low density accreting medium. Because of the low density, the medium is optically thin. The interaction rate between particles is low, so there is no efficient cooling mechanism: the gas temperature is very high, the gas is swallowed by the black hole without emitting much radiation, and the accretion luminosity is low.

Note that this is a schematic and simplified classification, and the above models have some overlaps.

## 2.1 Novikov-Thorne disks

The Novikov-Thorne model is the standard framework for the description of geometrically thin and optically thick accretion disks around black holes. The main assumptions of the model are:

1. The accretion disk is geometrically thin ( $h/r \ll 1$ ).
2. The accretion disk is perpendicular to the black hole spin.
3. The inner edge of the disk is at the ISCO radius.
4. The motion of the particle gas in the disk is determined by the gravitational field of the black hole, while the impact of the gas pressure is ignored.

For the full list of assumptions and a detailed discussion, see e.g. [10, 106] and references therein. Here we point out a few important considerations.

Assumption 1 just points out that the Novikov-Thorne model must be applied to thin disks, even if it is often used for every black hole X-ray source, in part because it is the only simple analytic model on the market and in part because it is often difficult to estimate the Eddington-scaled mass accretion rate (in particular for AGN, where mass and distance are usually poorly constrained).

The validity of assumption 2 depends on the origin and the evolution of the system. The cases of stellar-mass black holes and of supermassive black holes are somewhat different. Let us first consider stellar-mass black holes. If the object is the final product of the supernova explosion of a heavy star in a binary, its spin should be orthogonal to the orbital plane of the binary in the case of a symmetric explosion without strong shocks and kicks [40]. A misalignment may be introduced by a non-symmetric supernova explosion and/or shocks and kicks, as well as in those systems formed through multi-body interactions (binary capture or replacement), where the orientation of the spin of the black hole and that of the orbital angular momentum of the binary are initially uncorrelated.

The inner part of the disk – which is the one important in spin measurements – may be in any case expected to be in the equatorial plane perpendicular to the spin of the compact object as a result of the Bardeen-Petterson effect [12, 73]. This mechanism works for thin disks, because it requires  $\alpha > h/r$ , where  $\alpha \sim 0.01-0.1$  is the viscosity parameter. The combination of the Lense-Thirring precession with the disk viscosity eventually drags the innermost part of the disk into alignment with the black hole spin. Because of the short range of the Lense-Thirring effect, the outer part tends to remain in its original configuration. “Bardeen-Petterson configuration” refers to a system in which the inner part of the disk is flat and perpendicular to the black hole spin, while the outer part is also flat but in the plane perpendicular to the angular momentum vector of the binary.

The alignment timescale of thin disks has been estimated to be in the range  $10^6-10^8$  yrs, and therefore the disk should be already adjusted in the black hole equatorial plane for not too young systems [133] (but see [83, 84] for more details). However, the actual timescale depends on some unknown parameters, like the viscosity  $\alpha$ , [67, 78] and it should be noted that at least some numerical simulations do not find the adjustment of the disk [39, 171]. If the inner part of the disk is a hot, geometrically thick accretion flow, the picture is different and the inner disk precesses as a solid body [62]. Future X-ray spectropolarimetric measurements of the thermal spectrum of accretion disks will be able to check the validity of the assumption that the disk is in the equatorial plane (see, for instance, [10] and references therein).

In the case of supermassive black holes, the orientation of the accretion disk with respect to the black hole spin is expected to change during the evolution of the system, in particular because of galaxy merger processes. However, the Bardeen-Petterson effect should have had the time to make the inner part of the disk orthogonal to the black hole spin in the case of prolonged disk accretion.

The assumption that the inner edge of the disk is at the ISCO radius has a crucial role in the spin measurements via the continuum-fitting and the iron line methods. This is because, assuming the Kerr metric, there is a one-to-one correspondence between the spin parameter  $a_*$  and the ISCO radius  $r_{\text{ISCO}}$  (see previous chapter), and the exact position of the inner edge of the disk has a strong impact on the features of the spectrum. Observations show that the inner edge of the disk does not change appreciably over several years when the source is in the soft state (see Section 3 for the definition of soft state) with a luminosity between 5% to 30% of its Eddington limit. The most compelling evidence comes from LMC X-3. The analysis of many

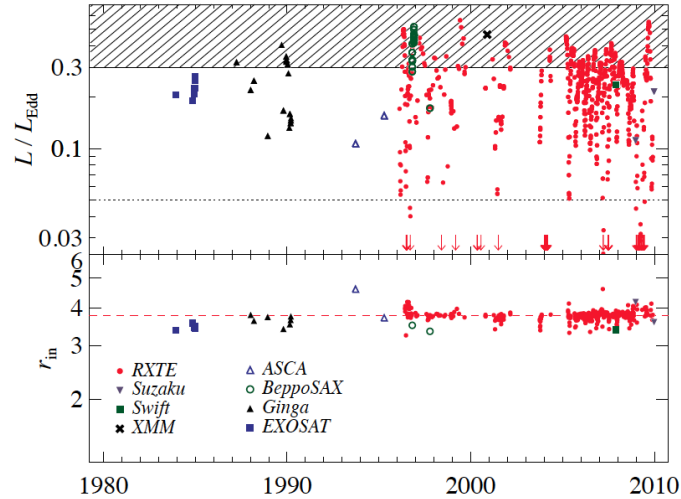


Fig. 5: Top panel: Accretion disk luminosity in Eddington units versus time for 766 spectra of LMC X-3. The shaded region does not satisfy the thin disk selection criterion  $L/L_{\text{Edd}} < 0.3$ , as well as the data below the dotted line, which marks  $L/L_{\text{Edd}} = 0.05$ . Bottom panel: fitted value of the inner disk radius of the 411 spectra in the top panel that can meet the thin disk selection criterion. See the text for more details. From [135]. ©AAS. Reproduced with permission.

spectra collected during eight X-ray missions and spanning 26 years shows that the radius of the inner edge of the disk is quite constant [135], see Fig. 5. The most natural interpretation is that the inner edge is associated to some intrinsic property of the geometry of the spacetime, namely the radius of the ISCO, and is not affected by variable phenomena like the accretion process.

Assumption 4 requires that the radial acceleration of the gas due to pressure gradients is negligible in comparison with the gravitational acceleration due to the black hole. This requires that, as the gas falls onto the black hole, its potential energy is transported away or radiated away, and only a negligible part is converted to internal energy of the gas [106]. This is true in the case of radiatively efficient accretion flow and it is the case for thin disks.

The accretion process in the Novikov-Thorne model can be summarized as follows. The particles of the accreting gas slowly fall onto the central black hole. When they reach the ISCO radius, they quickly plunge onto the black hole without emitting additional radiation. The total power of the accretion process is  $L = \eta \dot{M} c^2$ , where  $\eta = \eta_r + \eta_k$  is the total efficiency,  $\eta_r$  is the radiative efficiency, and  $\eta_k$  is the fraction of gravitational energy converted to kinetic energy of jets/outflows. The Novikov-Thorne model assumes that  $\eta_k$  can be ignored, and therefore the radiative

efficiency of a Novikov-Thorne accretion disk is

$$\eta_{\text{NT}} = 1 - E_{\text{ISCO}}, \quad (2)$$

where  $E_{\text{ISCO}}$  is the energy per unit rest-mass of the gas at the ISCO radius. The plot in Fig. 3 in the previous chapter shows  $\eta_{\text{NT}}$  as a function of the spin parameter  $a_*$ .

In spin measurements, it is clearly very important to select the observations and the sources in which the disk is geometrically thin and its inner edge is at the ISCO radius. In the case of the continuum-fitting method, one usually selects sources in the soft state with a strong contribution from the thermal disk emission. The luminosity of the source should be between  $\sim 5\%$  and 20-30% of the Eddington limit [87]. At lower luminosities, the disk may be truncated. In such a case, the inner edge of the disk would be at a radius larger than the ISCO and between the inner edge of the disk and the black hole there is probably an accretion flow that can be described by ADAF. For higher accretion rates, the gas pressure becomes more important, and the disk becomes slim. In such a case, the inner edge of the disk might be at a radius slightly smaller than the ISCO.

## 2.2 Disk-corona model

The disk-corona model is schematically illustrated in Fig. 6. The black hole accretes from a geometrically thin and optically thick disk. The disk emits as a blackbody locally and as a multi-color blackbody when integrated radially<sup>4</sup> (*thermal component* indicated by the red arrows in Fig. 6) [96]. For a given radius of the disk, the temperature depends on the black hole mass and the mass accretion rate. The peak temperature is reached near the inner edge of the disk and is in the soft X-ray band (0.1-1 keV) for stellar-mass black holes and in the optical/UV band (1-10 eV) for supermassive black holes.

The *corona* is a hotter ( $\sim 100$  keV), usually compact and optically thin, cloud close to the black hole, but its exact geometry is currently unknown [56, 118, 32]. Fig. 7 shows some proposed corona geometries. The lamppost corona is a point-like source along the spin axis of the black hole [29]. Such a possibility may be realized in the case the corona is the base of the jet. In the sandwich geometry, the corona would be the atmosphere above the accretion disk [57]. In the cases of a spherical or toroidal geometries, the corona would be the accretion flow between the inner edge of the disk and the black hole. The inverse Compton scattering of the thermal photons from the accretion disk off free electrons in the corona produces a *power-law component* (or *Comptonized component*, blue arrows in Fig. 6) with a cut-off

<sup>4</sup> Every point in the accretion disk is in local thermal equilibrium, and therefore we can define an effective temperature  $T_{\text{eff}}$  [in the case of an axisymmetric system,  $T_{\text{eff}} = T_{\text{eff}}(r)$  depends only on the radial coordinate]. Different points have a different temperature, and therefore we speak about “multi-color” or “multi-temperature” spectrum. The gas temperature increases as the gas particles fall into the gravitational potential of the black hole and transform potential energy into kinetic and internal energy.

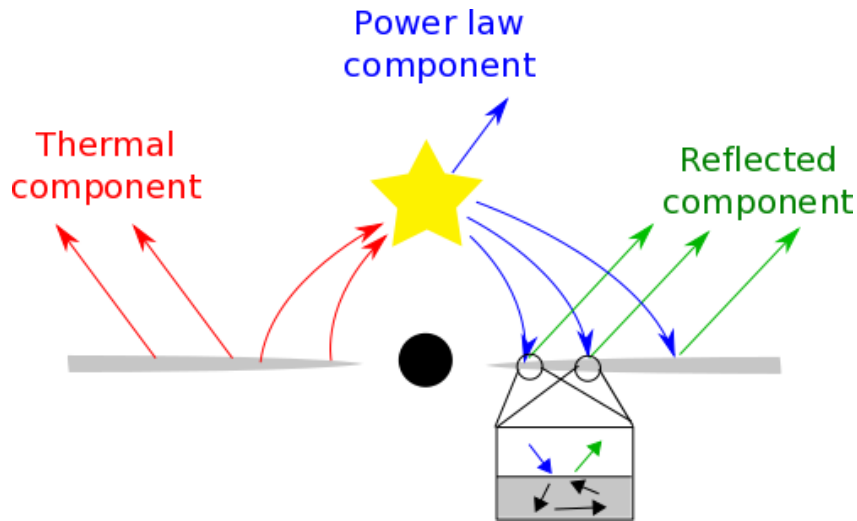


Fig. 6: Disk-corona model. The black hole is surrounded by a thin accretion disk with a multi-color blackbody spectrum (red arrows). Some thermal photons from the disk have inverse Compton scattering off free electrons in the corona, producing a power-law component (blue arrows). The latter also illuminates the disk, generating a reflection component (green arrows).

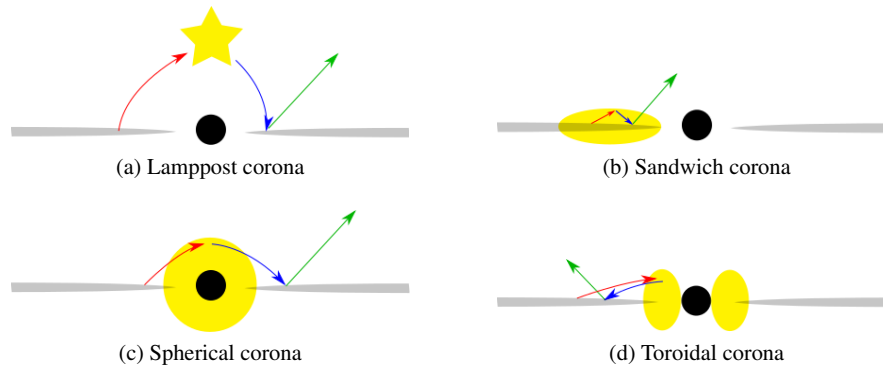


Fig. 7: Examples of possible corona geometries: lamppost geometry (top left panel), sandwich geometry (top right panel), spherical geometry (bottom left panel), and toroidal geometry (bottom right panel).

energy that depends on the temperature of the corona ( $E_{\text{cut}} \sim 100\text{-}1000$  keV) [142, 143].

The power-law component from the corona illuminates also the accretion disk, producing a *reflection component* (green arrows in Fig. 6) with some fluorescent emission lines [44]. The strongest feature of the reflection component is usually the

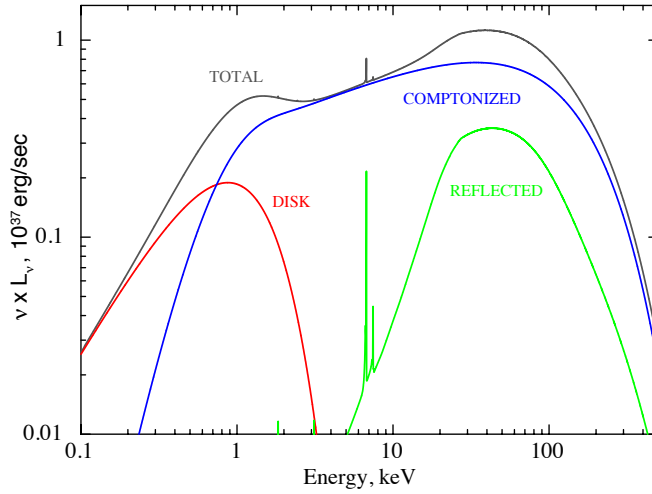


Fig. 8: Spectral components of an accreting black hole in the disk-corona model: disk’s thermal spectrum (red), power-law component from the corona (blue), and reflection component from the illumination of the disk by the power-law component (green).

iron  $K\alpha$  line, which is at 6.4 keV in the case of neutral or weakly ionized iron and shifts up to 6.97 keV for H-like iron ions, and the Compton hump at 10-30 keV.

Fig. 8 shows the resulting spectrum of the disk-corona geometry: we have the thermal component from the accretion disk, the power-law component from the corona, and the reflection component from the illumination of the accretion disk by the power-law component. In the presence of jets, we have also a jet component in the radio/IR bands due to synchrotron radiation emitted by particles accelerated in jets, but it may also extend to the X-ray and  $\gamma$ -ray bands.

### 3 Spectral state classification

An accreting black hole can be found in different “spectral states”, which are characterized by the luminosity of the source and by the relative contribution of its spectral components (thermal, power-law, reflection) [15, 60]. The spectral state classification is purely phenomenological, i.e. follows from the observed X-ray spectrum.

However, there should be a correlation (not completely understood as of now) between spectral states and accretion flow configurations.

Let us start discussing the case of a stellar-mass black hole in an X-ray transient. The object typically spends most of the time in a *quiescent state* with a very low accretion luminosity ( $L/L_{\text{Edd}} < 10^{-6}$ ). At a certain point, the source has an *outburst* and becomes a bright X-ray source in the sky ( $L/L_{\text{Edd}} \sim 10^{-3}$ -1). The quiescent state is determined by a very low mass accretion rate, namely a very low amount of material transfers from the companion star to the black hole. When there is a sudden increase of the mass accretion rate (for instance, the companion star inflates and the black hole strips material from the surface of the companion), there is the outburst. The object may be in a quiescent state for several months or even decades. An outburst typically lasts from some days to a few months (roughly the time that the black hole takes to swallow the material that produced the outburst). During an outburst, the spectrum of the source changes.

The *hardness-intensity diagram* (HID) [15, 60] is a useful tool for the description of an outburst, see Fig. 9. The  $x$ -axis is for the hardness of the source, which is the ratio between its luminosity in the hard and soft X-ray bands, for instance between the luminosity in the 6-10 and 2-6 keV bands, but other choices are also common. The  $y$ -axis can be for the X-ray luminosity or the count number of the instrument, but other choices are also possible. The hardness-intensity diagram depends on the source (e.g. the interstellar absorption) and on the instrument (e.g. its effective area at different energies), but, despite that, it turns out to be very useful to study transient sources.

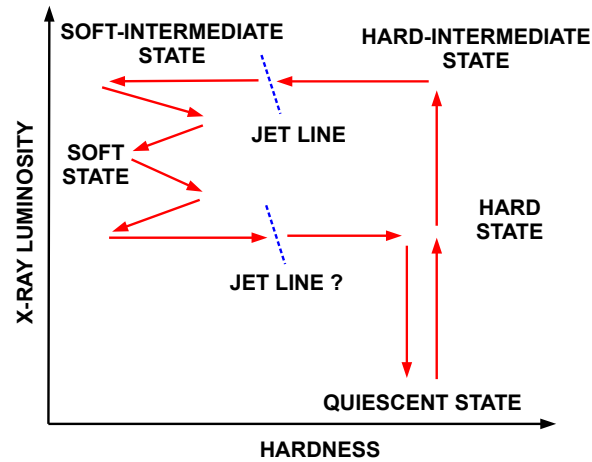


Fig. 9: Evolution of the prototype of an outburst in the hardness-intensity diagram. The source is initially in a quiescent state. At the beginning of the outburst, the source enters the hard state, then moves to some intermediate states, to the soft state, and eventually returns to a quiescent state. See the text for more details.



The relation between spectral states and accretion flow can be understood noting that the intensity of the thermal component is mainly determined by the mass accretion rate and the position of the inner edge of the accretion disk, while the contributions of the power-law and reflection components depend on the properties of the corona (its location, extension, geometry, etc.). In particular, the local flux of the disk's thermal component is approximately proportional to the mass accretion rate and the inverse of the cube of the disk's radius,  $\mathcal{F}(r) \propto \dot{M}/r^3$  [74]. When the mass accretion rate is low (high) and the inner edge of the disk is at large (small) radii, the thermal component is weak (strong). The power-law and the reflection components are strong (weak) when the corona is large (small) and close to (far from) the disk. The relative contribution of these three components depends on the material around the black hole, and, in turn, determines the spectral state.

*Quiescent state* — The source is initially in a quiescent state: the mass accretion rate and the luminosity are very low (the source may also be too faint to be detected) and the spectrum is hard. The inner edge of the accretion disk is truncated at a radius significantly larger than the ISCO and the accretion process around the black hole is described by ADAF. In this phase, the low-density accretion flow close to the black hole may act as the corona, which would thus be spherical and large.

*Hard state* (or corona-dominated state) — At the beginning of the outburst, the spectrum is hard and the source becomes brighter and brighter because the mass accretion rate increases ( $L/L_{\text{Edd}}$  starts from  $\sim 10^{-3}$  and can reach values up to  $\sim 0.7$  in some cases). The spectrum is dominated by the power-law and reflection components. The thermal component is subdominant, and the temperature of the inner part of the disk may be low, around 0.1 keV or even lower, but it increases as the luminosity of the source rises. The inner edge of the disk is initially at a radius larger than the ISCO one, but it moves to the ISCO as the luminosity increases, and it may be at the ISCO at the end of the hard state. During the hard state, compact mildly relativistic steady jets are common, but the exact mechanism producing these jets is currently unknown. Observations point out a compact corona [118, 32], which may be the base of the jet in a lamppost geometry.

*Intermediate states* — The mass accretion rate rises, so the contribution of the thermal component increases. The power-law and the reflection components get weaker, probably because of a variation in the geometry/properties of the corona. As a consequence, the source moves to the left part of the HID. We first have the *hard-intermediate state* and then the *soft-intermediate state*. As shown in Fig. 9, there exists a *jet line*, not well understood for the moment, in the HID: when the source crosses the jet line, we observe transient highly relativistic jets. Even in this case, the mechanism responsible for the production of these jets is unknown. If the hardness of the source oscillates near the jet line, we can observe several transient jets.

*Soft state* (or disk-dominated state) — The thermal spectrum of the disk is the dominant component in the spectrum and the inner part of the disk temperature is around 1 keV. If the luminosity of the source is between 5% to 20-30% of its Eddington luminosity, the inner edge of the disk should be at the ISCO radius [87], and the accretion disk should be well described by the Novikov-Thorne model [112,

72]. In the soft state, we do not observe any kind of jet<sup>5</sup>. However, strong winds and outflows are common (while they are absent in the hard state). The luminosity of the source may somewhat decrease and change hardness, remaining on the left side of the HID.

At a certain point, the transfer of material decreases, leading to the end of the outburst. The contribution of the thermal spectrum of the disk decreases and, as a consequence, the hardness of the source increases. The source re-enters the soft-intermediate state, the hard-intermediate state, then the hard state, and eventually, when the hardness is high, the luminosity drops down and the source returns to the quiescent state till the next outburst. Between the soft-intermediate and the hard-intermediate states, we may observe transient jets, but the existence of a jet line is not clear here. Every source follows the path shown in Fig. 9 counter-clockwise, but there are differences among different sources and even for the same source among different outbursts.

In the case of stellar-mass black holes in persistent X-ray sources, there is no outburst, but we can still use the HID. The most studied source is Cygnus X-1 (the other persistent sources are in nearby galaxies, so they are fainter and more difficult to study). This object spends most of the time in the hard state, but it occasionally moves to a softer state, which is usually interpreted as a soft state. LMC X-1 is always in the soft state. LMC X-3 is usually observed in the soft state, rarely in the hard state, and there is no clear evidence that this source can be in an intermediate state.

In the case of supermassive black holes, there are at least two important differences. First, the size of the system, which scales as the mass. 1 day for a  $10 M_{\odot}$  black hole corresponds to 3,000 years for a  $10^7 M_{\odot}$  black hole, which makes impossible the study of the evolution of a specific system. Second, the temperature of the disk is in the optical/UV range for a supermassive black hole. Despite these two issues, stellar-mass and supermassive black holes have a similar behavior and we can employ the same spectral state classification (see, for instance, [15] and references therein).

## 4 AGN classification

Active galactic nuclei (AGN) are very bright galactic nuclei, powered by the mass accretion onto their central supermassive black hole. The term AGN is usually used to indicate the same supermassive black hole as well.

Fig. 10 shows the AGN classification, groups and subgroups, and the corresponding fraction of members. While it is thought that most galaxies have a supermassive black hole at their center, only a small fraction of them host an AGN. In most galaxies, the central supermassive object is “dormient”, like the supermassive black hole

---

<sup>5</sup> For instance, in the corona lamppost geometry, the corona may be the base of the jet. This could explain why, in the soft state, we do not see jets and the power-law and reflection components are weak.

in the Galaxy, SgrA\*, which has a luminosity of the order of  $10^{-7}$  in Eddington units.

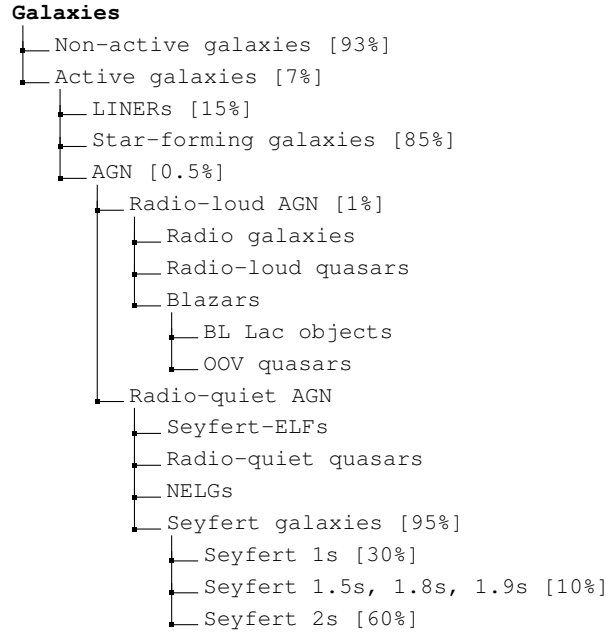


Fig. 10: Sketch of the AGN family and of its subgroups. This classification has to be taken with caution, because different authors may use slightly different classifications. The diagram shows also the fraction of members in each subgroup. AGN represent only 0.035% of the galactic nuclei. Most of the AGN are radio-quiet and belong to the class of Seyfert galaxies.

About 93% of the galaxies are non-active. Among the 7% of the active galaxies, most of them are star-forming galaxies or low-ionization nuclear emission-line regions (LINERs). The latter are sometimes considered AGN. Proper AGN are relatively rare: they are in 0.5% of the active galaxies, which means only in 0.035% of all galaxies.

AGN are mainly classified according to their luminosity and spectral features. It is thus useful to briefly review their possible spectral components:

1. *Radio emission* from jets with the typical spectrum from synchrotron radiation.
2. *IR emission* from the thermal spectrum of the accretion disk, which is reprocessed by gas and dust around the nucleus. This occurs when the accretion disk is obscured by gas and dust.
3. *Optical continuum* mainly from the thermal spectrum of the accretion disk, and in part from possible jets.

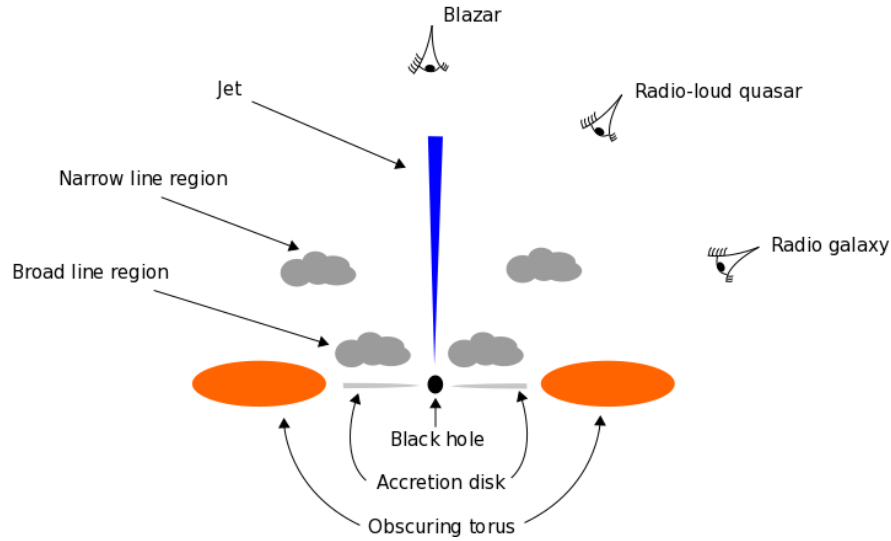


Fig. 11: Sketch of a radio-loud AGN according to the unified AGN model [150]. The black hole is surrounded by an accretion disk, which may be obscured by a dusty torus. The broad line region is close to the black hole and there are clouds orbiting with high velocity. The narrow line region is relatively far from the black hole and there are clouds moving at lower velocity. Depending on the angle between the jet and the line of sight of the observer, the AGN can appear as a blazar, as a radio-loud quasar, or as a radio galaxy, as shown in the picture.

4. *Narrow optical lines* from cold material orbiting relatively far from the supermassive black hole. The orbital velocity of this material is 500-1,000 km/s.
5. *Broad optical lines* from cold material orbiting close to the supermassive black hole. The orbital velocity of this material is 1,000-5,000 km/s. The lines are broad due to Doppler boosting.
6. *X-ray continuum* from a hot corona and possible jets.
7. *X-ray lines* from fluorescence emission of the gas in the accretion disk illuminated by the X-ray continuum. The iron  $K\alpha$  line at 6.4 keV is usually one of the most prominent lines.

The AGN classification is sometimes confusing, some objects may not be easily associated to a specific group, and different authors may use different classifications. With reference to Fig. 10, we see that AGN can be grouped into two classes, radio-quiet and radio-loud AGN. In radio-quiet AGN, the jet component is absent or negligible, so the radio luminosity is low. Radio-loud AGN have powerful jets. These jets may be powered by the black hole spin.

Radio-quiet AGN may be grouped into four classes: Seyfert extremely luminous far infrared galaxies (Seyfert-ELFs), Seyfert galaxies, narrow emission line galax-

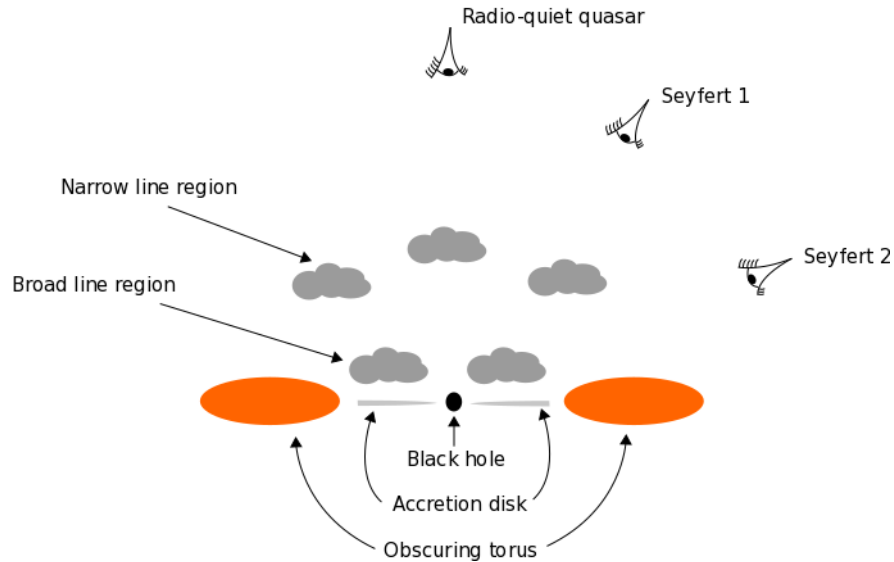


Fig. 12: As in Fig. 11, in the case of a radio-quiet AGN. Depending on the viewing angle of the observer, the AGN can appear as a radio-quiet quasar, as a Seyfert 1 galaxy, or as a Seyfert 2 galaxy.

ies (NELGs), and radio-quiet quasars. The classification is based on a number of properties. For instance, Seyfert galaxies have an optical continuum and emission lines. Seyfert 1s have both narrow and broad emission lines, while Seyfert 2s have only narrow emission lines. Seyfert galaxies of type 1.5, 1.8, and 1.9 are grouped according to their spectral appearance.

Radio-loud AGN can be grouped into three classes: radio galaxies, radio-loud quasars, and blazars. Blazars are characterized by rapid variability and by polarized optical, radio and X-ray emission. They are divided into BL Lacertae objects (BL Lac objects) and optically violent variable quasars (OVV quasars). OVV quasars have stronger broad emission lines than BL Lac objects.

According to the unified AGN model [150], all AGN would essentially belong to the same class of objects. They look different because they are observed from different viewing angles. Figs. 11 and 12 illustrate the idea of the unified AGN model. In the case of blazars, the jet would be along our line of sight. As the angle between the jet and our line of sight increases, we would have radio-loud quasars and then radio galaxies. In the case of radio-quiet AGN (Fig. 12), we have a similar situation, even if there is no jet: depending on the viewing angle of the observer, the AGN can appear as a radio-quiet quasar, as a Seyfert 1 galaxy, or as a Seyfert 2 galaxy.

## 5 Black hole spins

Generally speaking, the value of the spin parameter of a black hole can be expected to be determined by the competition of three physical processes: the event creating the object, mergers, and gas accretion.

### 5.1 *Stellar-mass black holes*

In the case of black hole binaries, it is usually thought that the spin of a black hole is mainly natal and that the effect of the accretion process is negligible [66]. However, see Ref. [41] for a different conclusion. The argument is that a stellar-mass black hole has a mass around  $10 M_{\odot}$ . If the stellar companion is a few Solar masses, the black hole cannot significantly change its mass and spin angular momentum even swallowing the whole star. If the stellar companion is heavy, its lifetime is too short: even if the black hole accretes at the Eddington rate, there is not the time to transfer the necessary amount of matter to significantly change the black hole spin parameter. One may expect that a black hole cannot swallow more than a few  $M_{\odot}$  from the companion star, and for a  $10 M_{\odot}$  object this is not enough to significantly changes  $a_*$  [66].

If the black hole spin were mainly natal, its value should be explained by studying the gravitational collapse of massive stars. While there are still uncertainties in the angular momentum transport mechanisms of the progenitors of stellar-mass black holes, it is widely accepted that the gravitational collapse of a massive star with Solar metallicity cannot create fast-rotating remnants [163, 167]. The birth spin of these black holes is expected to be low (see e.g. [41] and references therein). However, this is not what we observe. For instance, in the case of LMXBs, the black hole in GRS 1915+105 has  $a_* > 0.98$  [87] and  $M = 12.4 \pm 2.0 M_{\odot}$  [115], while the stellar companion's mass is  $M = 0.52 \pm 0.41 M_{\odot}$ . In the case of HMXBs, the black hole in Cygnus X-1 has  $a_* > 0.98$  [54, 55] and  $M = 14.8 \pm 1.0 M_{\odot}$ , while the stellar wind from the companion is not an efficient mechanism to transfer mass. Very high spin values are also measured for GS 1354-645, MAXI J1535-571, and Swift J1658.2, see Tab. 2.

While black holes in LMXBs and HMXBs should form in different environments, in both cases the origin of so high spin values is not well understood. In Ref. [41], the authors show indeed that the accretion process immediately after the formation of a black hole binary may be very important and eventually responsible for the high spins of black holes in LMXBs.

## 5.2 Supermassive black holes

The case of supermassive black holes in galactic nuclei is different. The initial value of their spin parameter is likely completely irrelevant: their mass has increased by several orders of magnitude from its original value, and the spin parameter has evolved accordingly. On average, the capture of small bodies (minor merger) in randomly oriented orbits should spin the compact object down, since the magnitude of the orbital angular momentum for corotating orbits is always smaller than the one for counterrotating orbits [61]. In the case of random merger of two black holes with comparable mass (major merger), the most probable final product is a black hole with  $a_* \approx 0.70$ , while fast-rotating objects with  $a_* > 0.9$  should be rare [16].

Accretion from a disk can potentially be a very efficient way to spin a compact object up [16]. If accretion proceeds via short episodes (chaotic accretion) [68], the net effect is not different from minor mergers in randomly oriented orbits and the compact object is spun down. On the contrary, prolonged disk accretion is a very efficient mechanism to spin the compact object up. In this case, black holes in AGN may have a spin parameter close to the Thorne limit [16] (see next section). Such a possibility seems to be supported by some observations; see e.g. Ref. [161] and also the spin measurements from X-ray reflection spectroscopy in Tab. 3. Nearby supermassive black holes accreting from a more spherically symmetric gas distribution may instead have lost most of their spin angular momentum acquired in a previous stage and have lower spin, or they may be in the process of spinning down.

## 5.3 Thorne limit

An accreting black hole changes its mass  $M$  and spin angular momentum  $J$  as it swallows more and more material from its disk. In the case of a Novikov-Thorne disk, it is relatively easy to calculate the evolution of these parameters. If we assume that the gas in the disk emits radiation until it reaches the ISCO radius and then quickly plunges onto the black hole, the evolution of the spin parameter  $a_*$  is governed by the following equation [147]

$$\frac{da_*}{d \ln M} = \frac{c}{r_g} \frac{L_{\text{ISCO}}}{E_{\text{ISCO}}} - 2a_*, \quad (3)$$

where  $E_{\text{ISCO}}$  and  $L_{\text{ISCO}}$  are, respectively, the energy and the angular momentum per unit rest-mass of the gas at the ISCO radius. Assuming an initially non-rotating black hole of mass  $M_0$ , the solution of Eq. (3) is

$$a_* = \begin{cases} \sqrt{\frac{2}{3}} \frac{M_0}{M} \left[ 4 - \sqrt{18 \frac{M_0^2}{M^2} - 2} \right] & \text{if } M \leq \sqrt{6} M_0, \\ 1 & \text{if } M > \sqrt{6} M_0. \end{cases} \quad (4)$$

The black hole spin parameter  $a_*$  monotonically increases from 0 to 1 and then remains constant.  $a_* = 1$  is the equilibrium spin parameter and is reached after the black hole has increased its mass by the factor  $\sqrt{6} \approx 2.4$ .

If we take into account the fact that the gas in the accretion disk emits radiation and that a fraction of this radiation is captured by the black hole, Eq. (3) becomes [147]

$$\frac{da_*}{d \ln M} = \frac{c}{r_g} \frac{L_{\text{ISCO}} + \zeta_{\text{L}}}{E_{\text{ISCO}} + \zeta_{\text{E}}} - 2a_*, \quad (5)$$

where  $\zeta_{\text{L}}$  and  $\zeta_{\text{E}}$  are related to the amount of photons captured by the black holes and must be computed numerically. Now the equilibrium value of the spin parameter is not 1 but the so-called *Thorne limit*  $a_*^{\text{Th}} \approx 0.998$  (its exact numerical value depends on the emission properties of the gas in the disk) [147]. The Thorne limit is lower than 1 because photons with angular momentum antiparallel to the black hole spin have larger capture cross section and therefore they contribute to spin the black hole down.

## 6 Techniques for measuring black hole spins

Any astrophysical black holes should be completely characterized by its mass  $M$  and its spin parameter  $a_*$ . It is relatively easy to measure the mass of a black hole, by studying the orbital motion of gas or of individual stars around the compact object. Spin measurements are much more challenging. The spin has no “gravitational effects” in Newtonian gravity. This is not the case in general relativity, and the spin alters the gravitational field around a massive body. However, any spin effect is strongly suppressed at larger radii, so black hole spin measurements require to probe the strong gravity region near the black hole event horizon. As of now, there are two leading techniques to measure black hole spins by studying the X-ray radiation emitted by the gas in the inner part of the accretion disk: the so-called *continuum-fitting method*, which consists in the analysis of the thermal spectrum of thin accretion disks and is usually applicable to stellar-mass black holes only, and *X-ray reflection spectroscopy* (or *iron line method*), which is based on the study of the disk’s reflection spectrum, can be applied to both stellar-mass and supermassive black holes, and is currently the only available method to measure the spins of supermassive black holes. There are a few other proposed techniques for measuring black hole spins with electromagnetic radiation. Among these, the most promising one is probably the detection of *quasi-periodic oscillations* (QPOs).



### 6.1 Continuum-fitting method

Within the Novikov-Thorne model, we can derive the time-averaged radial structure of the accretion disk from the fundamental laws of the conservation of rest-mass, energy, and angular momentum [106]. The time-averaged energy flux emitted from the surface of the disk is

$$\mathcal{F}(r) = \frac{\dot{M}c^2}{4\pi r_g^2} F(r), \quad (6)$$

where  $\dot{M} = dM/dt$  is the time-averaged mass accretion rate, which is independent of the radial coordinate, and  $F(r)$  is a dimensionless function of the radial coordinate that becomes roughly of order 1 at the disk inner edge (see [106] for more details). Assuming that the disk is in local thermal equilibrium, its emission is blackbody-like and at any radius we can define an effective temperature  $T_{\text{eff}}(r)$  from the time-averaged energy flux as  $\mathcal{F} = \sigma T_{\text{eff}}^4$ , where  $\sigma$  is the Stefan-Boltzmann constant.

Novikov-Thorne disks with the inner edge at the ISCO radius are realized when the accretion luminosity is between 5% to 20-30% of the Eddington limit of the object [87], and this is confirmed by theoretical [112, 72] and observational studies [135]. At lower luminosities, the disk is more likely truncated at a radius larger than the ISCO, and we have an ADAF between the inner edge of the disk and the black hole. At higher luminosities, the gas pressure becomes important, the inner part of the disk is not thin any longer, and the inner edge might be at a radius slightly smaller than the ISCO [7]. Requiring  $\dot{M} \sim 0.1 \dot{M}_{\text{Edd}}$  as the condition for Novikov-Thorne disks, we can get a rough estimate of the effective temperature of the inner part of the accretion disk

$$T_{\text{eff}} \sim \left( \frac{0.1 \dot{M}_{\text{Edd}} c^2}{4\pi \sigma r_g^2} \right)^{1/4} \sim \left( \frac{10 M_{\odot}}{M} \right)^{1/4} \text{ keV}, \quad (7)$$

and we can see that the disk's thermal spectrum is in the soft X-ray band for stellar-mass black holes and in the optical/UV band for the supermassive ones.

The continuum-fitting method is the analysis of the thermal spectrum of geometrically thin and optically thick accretion disks of black holes in order to measure the black hole spin parameter  $a_*$  [170, 76, 88, 86]. The technique is normally used for stellar-mass black holes only, because the spectrum of supermassive black holes is in the optical/UV band where dust absorption limits the capability of accurate measurements.

The model describing the thermal spectrum of an accretion disk around a Kerr black hole depends on five parameters: the black hole mass  $M$ , the mass accretion rate  $\dot{M}$ , the inclination angle of the disk with respect to the line of sight of the observer  $i$ , the distance of the source from the observer  $D$ , and the black hole spin parameter  $a_*$ . The impact of these five parameters on the shape of the spectrum is illustrated in Fig. 13.

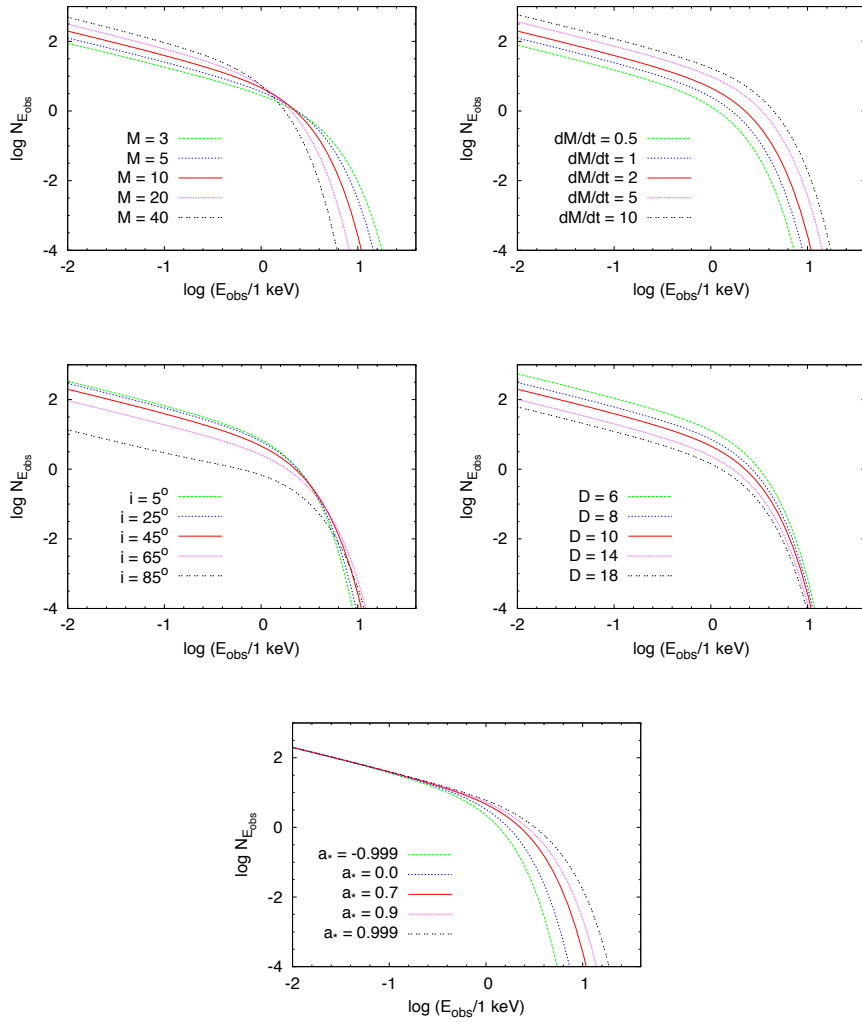


Fig. 13: Impact of the model parameters on the thermal spectrum of a thin disk: mass  $M$  (top left panel), mass accretion rate  $\dot{M}$  (top right panel), viewing angle  $i$  (central left panel), distance  $D$  (central right panel), and spin parameter  $a_*$  (bottom panel). When not shown, the values of the parameters are:  $M = 10 M_\odot$ ,  $\dot{M} = 2 \cdot 10^{18} \text{ g s}^{-1}$ ,  $D = 10 \text{ kpc}$ ,  $i = 45^\circ$ , and  $a_* = 0.7$ .  $M$  in units of  $M_\odot$ ,  $\dot{M}$  in units of  $10^{18} \text{ g s}^{-1}$ ,  $D$  in kpc, and flux density  $N_{E_{\text{obs}}}$  in photons  $\text{keV}^{-1} \text{ cm}^{-2} \text{ s}^{-1}$ .

Note that it is impossible to infer all the five model parameters from the data of the spectrum of a thin disk, because the spectrum's shape is too simple and there is a degeneracy. However, if we can get independent measurements of  $M$ ,  $D$ , and  $i$ ,

BH Binary	$a_*$ (Continuum)	$a_*$ (Iron)	Principal References
GRS 1915+105	$> 0.98$	$0.98 \pm 0.01$	[87, 92]
Cygnus X-1	$> 0.98$	$> 0.95$	[54, 55, 33, 149, 108, 160]
GS 1354-645	—	$> 0.98$	[30]
MAXI J1535-571	—	$> 0.98$	[165, 93]
Swift J1658.2	—	$> 0.96$	[166]
LMC X-1	$0.92 \pm 0.06$	$0.97^{+0.02}_{-0.25}$	[52, 139]
GX 339-4	$< 0.9$	$0.95 \pm 0.03$	[70, 117, 45, 109]
XTE J1752-223	—	$0.92 \pm 0.06$	[120, 46]
MAXI J1836-194	—	$0.88 \pm 0.03$	[119]
M33 X-7	$0.84 \pm 0.05$	—	[77]
4U 1543-47	$0.80 \pm 0.10^*$	—	[127]
IC10 X-1	$\gtrsim 0.7$	—	[137]
Swift J1753.5	—	$0.76^{+0.11}_{-0.15}$	[116]
XTE J1650-500	—	$0.84 \sim 0.98$	[158]
GRO J1655-40	$0.70 \pm 0.10^*$	$> 0.9$	[127, 116]
GS 1124-683	$0.63^{+0.16}_{-0.19}$	—	[25]
XTE J1652-453	—	$< 0.5$	[26]
XTE J1550-564	$0.34 \pm 0.28$	$0.55^{+0.15}_{-0.22}$	[138]
LMC X-3	$0.25 \pm 0.15$	—	[134]
H1743-322	$0.2 \pm 0.3$	—	[136]
A0620-00	$0.12 \pm 0.19$	—	[53]
XMMU J004243.6	$< -0.2$	—	[91]

Table 2: Summary of the continuum-fitting and iron line measurements of the spin parameter of stellar-mass black holes. See the references in the last column for more details. Note: \*These sources were studied in an early work of the continuum-fitting method, within a more simple model, and therefore the published 1- $\sigma$  error estimates are doubled following [86].

usually from optical observations, it is possible to fit the data and measure  $a_*$  and  $\dot{M}$ . This is the continuum-fitting method. Currently, there are about ten stellar-mass black holes with a spin measurement from the continuum-fitting method, see Tab. 2.

## 6.2 X-ray reflection spectroscopy

X-ray reflection spectroscopy (or iron line method) refers to the study of the reflection component. This technique can be applied to both stellar-mass and supermassive black holes and is currently the only available method to measure the spin of supermassive black holes [122, 20].

Object	$a_*$ (Iron)	Principal References
IRAS 13224-3809	$> 0.99$	[159]
Mrk 110	$> 0.99$	[159]
NGC 4051	$> 0.99$	[111]
1H0707-495	$> 0.98$	[159, 172]
RBS 1124	$> 0.98$	[159]
NGC 3783	$> 0.98$	[23]
NGC 1365	$0.97^{+0.01}_{-0.04}$	[124, 22]
Swift J0501-3239	$> 0.96$	[159]
PDS 456	$> 0.96$	[159]
Ark 564	$0.96^{+0.01}_{-0.06}$	[159]
3C120	$> 0.95$	[79]
Mrk 79	$> 0.95$	[42]
NGC 5506	$0.93^{+0.04}_{-0.04}$	[141]
MCG-6-30-15	$0.91^{+0.06}_{-0.07}$	[21, 82]
Ton S180	$0.91^{+0.02}_{-0.09}$	[159]
1H0419-577	$> 0.88$	[159]
IRAS 00521-7054	$> 0.84$	[144]
Mrk 335	$0.83^{+0.10}_{-0.13}$	[159, 107]
Ark 120	$0.81^{+0.10}_{-0.18}$	[159, 102]
Swift J2127+5654	$0.6^{+0.2}_{-0.2}$	[94]
Mrk 841	$> 0.56$	[159]
Fairall 9	$0.52^{+0.19}_{-0.15}$	[159, 126]

Table 3: Summary of spin measurements of supermassive black holes reported in the literature. See the references in the last column for more details.

The most prominent feature of the reflection spectrum is usually the iron  $K\alpha$  line<sup>6</sup>. This is because the iron is more abundant than other heavy elements (the iron-56 nucleus is more tightly bound than lighter and heavier elements, so it is the final product of nuclear reactions) and the probability of fluorescent line emission is also high (it scales as  $Z^4$ , where  $Z$  is the atomic number). Moreover, X-ray detectors have typically a good sensitivity around 6 keV and there are no other atomic lines around this energy. The iron  $K\alpha$  line is a very narrow feature in the rest-frame of the emitter, while the one observed in the reflection spectrum of black holes can be very broad and skewed, as the result of relativistic effects occurring in the strong gravity region of the object (gravitational redshift, Doppler boosting, light bending) [10, 122, 20,

<sup>6</sup> A  $K\alpha$  line results from the transition of an electron from a  $p$  orbit of the L shell (quantum number 2) to the K shell (quantum number 1). The line is actually a doublet with slightly different energies,  $K\alpha_1$  and  $K\alpha_2$ , respectively for the transitions  $2p_{1/2} \rightarrow 1s$  and  $2p_{3/2} \rightarrow 1s$  using the atomic notation. A  $K\beta$  line results from the transition of an electron from a  $p$  orbit of the M shell (quantum number 3) to the K shell. An  $L\alpha$  line is emitted from transition of an electron from a  $d$  orbit of the M shell to a  $p$  orbit of the L shell.

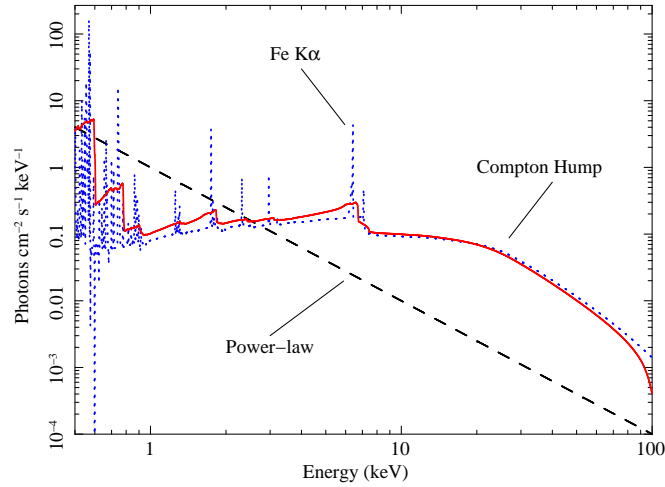


Fig. 14: Reflection spectrum for a neutral accretion disk irradiated by a power-law continuum with photon index  $\Gamma = 2$ . The dashed black line indicates the power-law continuum from the corona; the dotted blue curve is for the reflection spectrum at the emission point in the rest-frame of the gas (only atomic physics is involved); the solid red curve is for the reflection spectrum of a non-rotating black hole at the detection point and is blurred by relativistic effects (gravitational redshift, Doppler boosting, light bending). From [20], reproduced with permission.

31]. While the iron  $K\alpha$  line is usually the strongest feature, accurate measurements of black hole spins require to fit the whole reflection spectrum, not just the iron line. Fig. 14 shows the reflection spectrum for a neutral accretion disk: the unblurred reflection spectrum in the rest-frame of the gas is the dotted blue curve while the solid red curve is the blurred reflection spectrum of the accretion disk around a Schwarzschild black hole as detected by a distant observer.

Reflection models describing the reflection component of accretion disks around Kerr black holes depend on several parameters: the black holes spin  $a_*$ , the inner edge of the disk  $R_{\text{in}}$  (which may or may not be assumed at the ISCO radius), the outer edge of the disk  $R_{\text{out}}$ , the inclination angle of the disk  $i$ , the metallicity (or the iron abundance), the ionization of the disk, and some parameters related to the emissivity profile of the disk. The latter is quite a crucial ingredient and depends on the geometry of the corona, which is currently unknown. Coronas with arbitrary geometries can be modeled with a power-law emissivity profile (the intensity on the disk is  $I \propto 1/r^q$  where  $q$  is the emissivity index) or with a broken power-law ( $I \propto 1/r^{q_{\text{in}}}$  for  $r < R_{\text{br}}$ ,  $I \propto 1/r^{q_{\text{out}}}$  for  $r > R_{\text{br}}$ , and we have three parameters: the inner emissivity index  $q_{\text{in}}$ , the outer emissivity index  $q_{\text{out}}$ , and the breaking radius  $R_{\text{br}}$ ). In

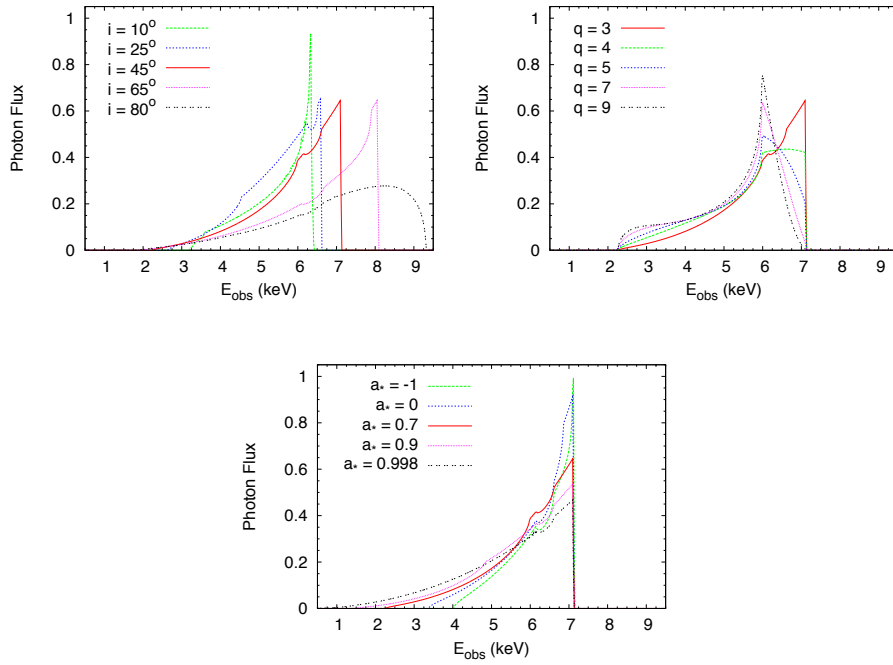


Fig. 15: Impact of the the inclination angle of the disk  $i$ , the emissivity index  $q$  (assuming an emissivity profile described by a simple power-law  $I \propto 1/r^q$ ), and the spin parameter  $a_*$  on the shape of an iron line at 6.4 keV emitted from a thin accretion disk. When not shown, the values of the parameters are:  $i = 45^\circ$ ,  $q = 3$ ,  $a_* = 0.7$ , and  $R_{\text{out}} = 400 r_g$ . From [10], reproduced with permission.

the case of supermassive black holes, it is often necessary to take the cosmological redshift  $z$  into account. For stellar-mass black holes, their relative motion in the Galaxy is of order 100 km/s and their Doppler boosting can be ignored. Fig. 15 shows the impact of the the inclination angle of the disk  $i$ , the emissivity index  $q$  (assuming an emissivity profile described by a simple power-law  $I \propto 1/r^q$ ), and the spin parameter  $a_*$  on the shape of an iron line at 6.4 keV emitted from a thin accretion disk around a black hole.

Note that spin measurements with the iron line method do not require independent measurements of the black hole mass  $M$ , the distance  $D$ , and the inclination angle of the disk  $i$ , three quantities that are required in the continuum-fitting method, are usually difficult to measure, and have large uncertainty. The reflection spectrum is independent of  $M$  and  $D$ , and can directly measure the inclination angle of the disk  $i$ .

Current spin measurements of stellar-mass black holes with the iron line method are summarized in the third column in Tab. 2 (see the corresponding references in

the fourth column for more details). Note that some black holes have their spin measured with both the continuum-fitting and the iron line methods. In general, the two measurements agree (GRS 1915+105, Cygnus X-1, LMC X-1, XTE J1550-564). For GX 339-4 and GRO J1655-40, the two measurements are not consistent. The iron line method is usually applied when the source is in the hard state, when the reflection spectrum is stronger but the disk may be truncated at a radius larger than the ISCO. This would lead to underestimate the black hole spin, and therefore it cannot be the case of the spin measurements of GX 339-4 and GRO J1655-40, where the iron line method provides spin values higher than the continuum-fitting method. As pointed out before, the continuum-fitting method crucially depends on independent measurements of the black hole mass  $M$ , the distance  $D$ , and the inclination angle of the disk  $i$ , three quantities that are usually difficult to measure and may be affected by large systematic uncertainties. For example, in the case of GRO J1655-40 there are a few mass measurements reported in the literature, but they are not consistent among them. Note, however, that the iron line measurement of GRO J1655-40 and the disk measurement of GX 339-4 are reported in some early work, based on more simple models, and the two measurements should probably be taken with more caution.

A summary of spin measurements of supermassive black holes with the iron line method is reported in Tab. 3 (see the references in the last column for more details and the lists of spin measurements in [122, 20, 153] for a few more sources with a constrained spin). Note the very high spin of several objects. In part, this can be explained noting that fast-rotating black holes are brighter and thus the spin measurement is easier. If these measurements are correct, they would point out that these objects have been spun up by prolonged disk accretion and therefore would provide information about galaxy evolutions (see the discussion in Section 5.3). However, the very high spin measurements have to be taken with some caution, as they may be affected by large systematic uncertainties in the model employed to infer the black hole spin. More details on the possible interpretation of current spin measurements of supermassive black holes can be found in [122].

### 6.3 Quasi periodic oscillations

Quasi-periodic oscillations (QPOs) are a common feature in the X-ray power density spectrum of neutron stars and stellar-mass black holes [152]. The power density spectrum  $P(\nu)$  is the square of the Fourier transform of the photon count rate  $C(t)$ . If we use the Leahy normalization, we have

$$P(\nu) = \frac{2}{N} \left| \int_0^T C(t) e^{-2\pi i \nu t} dt \right|^2, \quad (8)$$

where  $N$  is the total number of counts and  $T$  is the duration of the observation. QPOs are narrow features in the X-ray power density spectrum of a source. Fig. 16 shows

the power density spectrum obtained from an observation of the stellar-mass black hole XTE J1550-564, where we can see a QPO around 5 Hz, one at 13 Hz, and one at 183 Hz in the inset.

In the case of black hole binaries, QPOs can be grouped into two classes: low-frequency QPOs (0.1-30 Hz) and high-frequency QPOs (40-450 Hz). The exact nature of these QPOs is currently unknown, but there are several proposals in the literature. In most scenarios, the frequencies of the QPOs are related to the fundamental frequencies of a particle orbiting the black hole [140, 5, 6]:

1. *Orbital frequency*  $\nu_\phi$ , which is the inverse of the orbital period.
2. *Radial epicyclic frequency*  $\nu_r$ , which is the frequency of radial oscillations around the mean orbit.
3. *Vertical epicyclic frequency*  $\nu_\theta$ , which is the frequency of vertical oscillations around the mean orbit.

In the Kerr metric, we have a compact analytic form for the expression of these frequencies

$$\nu_\phi = \frac{c}{2\pi} \sqrt{\frac{r_g}{r^3}} \left[ 1 \pm a_* \left( \frac{r_g}{r} \right)^{3/2} \right]^{-1}, \quad (9)$$

$$\nu_r = \nu_\phi \sqrt{1 - 6 \frac{r_g}{r} \pm 8a_* \left( \frac{r_g}{r} \right)^{3/2} - 3a_*^2 \left( \frac{r_g}{r} \right)^2}, \quad (10)$$

$$\nu_\theta = \nu_\phi \sqrt{1 \mp 4a_* \left( \frac{r_g}{r} \right)^{3/2} + 3a_*^2 \left( \frac{r_g}{r} \right)^2}, \quad (11)$$

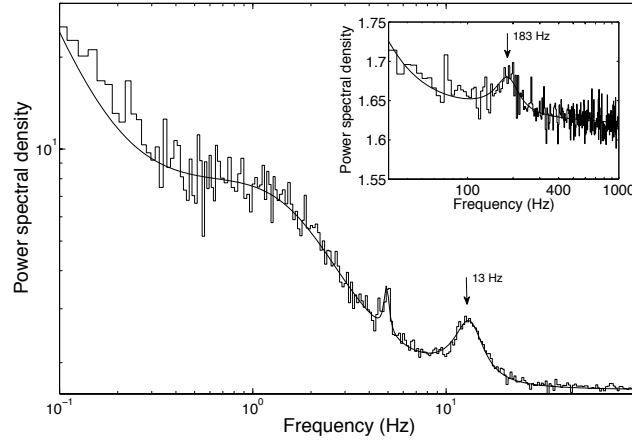


Fig. 16: Power density spectrum from an observation of XTE J1550-564. We see a QPO around 5 Hz, a QPO at 13 Hz (marked by an arrow), and a QPO at 183 Hz in the inset (marked by an arrow). Fig. 1 from [98], reproduced by permission of Oxford University Press.



where  $r$  is the orbital radius in Boyer-Lindquist coordinates. Since it is often possible to measure the frequencies of QPOs with quite a good precision, if we knew the exact relation between QPOs and fundamental frequencies, it could be possible to measure black hole spins with high precision. For instance, in Ref. [97] the authors interpret the observed QPOs of the black hole binary GRO J1655-40 within the relativistic precession model and obtain the mass measurement  $M/M_\odot = 5.31 \pm 0.07$  and the spin measurement  $a_* = 0.290 \pm 0.003$ .

To have an idea of the order of magnitude of these frequencies, we can write the orbital frequency for a Schwarzschild black hole

$$v_\phi(a_* = 0) = 220 \left( \frac{10M_\odot}{M} \right) \left( \frac{6r_g}{r} \right)^{3/2} \text{ Hz}. \quad (12)$$

High-frequency QPOs at 40-450 Hz are thus of the right magnitude to be associated to the orbital frequencies near the ISCO radius of stellar-mass black holes. Interestingly, we have evidence also of high-frequency QPOs in supermassive black holes ( $< 1$  mHz) [51] and intermediate-mass black holes ( $\sim 1$  Hz) [110].

## 7 Direct imaging

Depending on the geometry of the accretion disk and on its optical properties (thin/thick), if we could image the accretion flow around a black hole with a resolution of at least some gravitational radii, we would observe a dark area of a brighter background. The dark area is usually referred to as the black hole *shadow* [34] (see Fig. 17) and its boundary is determined by light bending in the strong gravity region [11].

Very long baseline interferometry (VLBI) facilities are the combination of several radio telescopes far each other that are used as a single telescope to reach much smaller angular resolutions. Sub-mm VLBI experiments promise to observe the shadow of the supermassive black hole at the center of the Galaxy very soon<sup>7</sup>. Its mass is about  $4 \cdot 10^6 M_\odot$  and it is at  $d \approx 8$  kpc from us, so its angular size in the sky is roughly

$$\theta \sim \frac{r_g}{d} \sim 0.05 \text{ milliarcseconds}. \quad (13)$$

There are three particular conditions that make the observation of the shadow of the black hole of the Galaxy achievable. *i)* The angular resolution of VLBI facilities scales as  $\lambda/D$ , where  $\lambda$  is the electromagnetic radiation wavelength and  $D$  is the distance among different stations. For  $\lambda < 1$  mm and stations located in different continents ( $D > 10^3$  km), it is possible to reach an angular resolution of 0.1 milliarcseconds. *ii)* The emitting medium around the black hole at the center of the

<sup>7</sup> <http://www.eventhorizontelescope.org/>

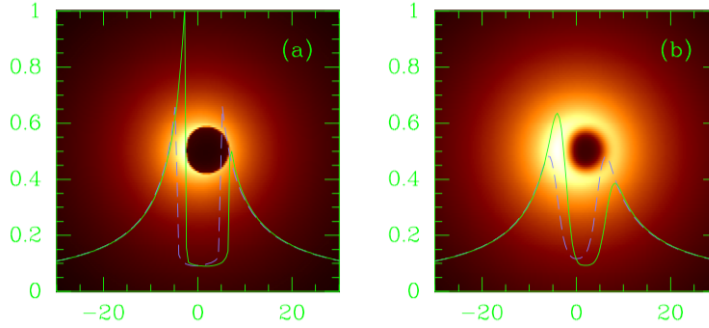


Fig. 17: Direct image of a black hole surrounded by an optically thin emitting medium with the characteristics of that of SgrA\*. The black hole spin parameter is  $a_* = 0.998$  and the viewing angle is  $i = 45^\circ$ . Panel *a*: image from ray-tracing calculations. Panel *b*: image from a simulated observation of an idealized VLBI experiment at 0.6 mm wavelength taking interstellar scattering into account. The solid green curve and the dashed purple curve show, respectively, the intensity variations of the image along the  $x$ -axis and the  $y$ -axis. From [34]. ©AAS. Reproduced with permission.

Galaxy is optically thick at wavelengths  $\lambda > 1$  mm, but becomes optically thin for  $\lambda < 1$  mm. *iii*) The interstellar scattering at the center of the Galaxy dominates over intrinsic source structures at wavelengths  $\lambda > 1$  mm, but becomes subdominant for  $\lambda < 1$  mm.

In the case of stellar-mass black holes in the Galaxy, the angular size is 4-5 orders of magnitude smaller. Similar angular resolutions are impossible today, but they may be possible in the future with X-ray interferometric techniques [162].

## 8 Jets

Jets are a common feature of several astrophysical objects, including protostars, stars, neutron stars, and black holes. Jets are observed both from stellar-mass black holes in X-ray binaries and supermassive black holes in galactic nuclei, see e.g. [95, 36, 169]. The exact mechanism responsible for the formation of black hole jets is currently unknown.

### 8.1 Theoretical models

The two most popular mechanisms for the formation of black hole jets are the Blandford-Znajek model [18] and the Blandford-Payne model [17], both with a

number of variants and extensions. There are also proposals of hybrid models, in which the two mechanisms can coexist [90].

In the *Blandford-Znajek scenario*, magnetic fields thread the black hole horizon and can extract the rotational energy of the compact object [18]. This mechanism exploits the existence of the ergoregion via the Penrose process [113]. However, strictly speaking, the extraction of the rotational energy of a compact object may be possible even in the case of neutron stars in the presence of magnetic fields anchored on the surface of the body.

In the original paper by Blandford and Znajek, the jet power  $P_{\text{BZ}}$  was derived assuming  $a_* \ll 1$ . In that case, one finds  $P_{\text{BZ}} \propto a_*^2$ . A more detailed analysis provides the following formula [145]

$$P_{\text{BZ}} = \frac{\kappa}{16\pi} \Phi_{\text{B}}^2 \Omega_{\text{H}}^2 f(\Omega_{\text{H}}), \quad (14)$$

where  $\kappa$  is a constant that depends on the magnetic field configuration,  $\Omega_{\text{H}}$  is the angular frequency at the black hole horizon and reads

$$\Omega_{\text{H}} = \frac{ca_*}{2r_{\text{H}}} = \frac{c}{2r_{\text{g}}} \frac{a_*}{1 + \sqrt{1 - a_*^2}}, \quad (15)$$

$\Phi_{\text{B}}$  is the magnetic flux threading the black hole horizon, and  $f(\Omega_{\text{H}})$  is a dimensionless function that takes into account higher order terms in  $\Omega_{\text{H}}$

$$f(\Omega_{\text{H}}) \approx 1 + c_1 \Omega_{\text{H}}^2 + c_2 \Omega_{\text{H}}^4 + \dots, \quad (16)$$

where  $\{c_i\}$  are numerical coefficients and this last formula assumes units in which  $M = c = 1$ . For a black hole with a thin accretion disk,  $c_1 = 1.38$  and  $c_2 = -9.2$  [145].

In the *Blandford-Payne model*, magnetic fields thread the accretion disk, corotating with it [17]. Now the energy is provided by the gravitational potential energy of the accretion flow. The power of the jet can be written as

$$P_{\text{BZ}} \sim \varepsilon L \ln \left( \frac{r_{\text{out}}}{r_{\text{in}}} \right), \quad (17)$$

where  $\varepsilon$  is the efficiency of the transformation of the binding energy of the accreting matter into jet power at the inner radius of the disk  $r_{\text{in}}$ ,  $r_{\text{out}}$  is the outer radius of the disk, and  $L$  is the accretion luminosity.

## 8.2 Observations

### 8.2.1 Stellar-mass black holes

In the case of black hole binaries, we observe two kinds of jets [36]. *Steady jets* manifest when a source is in the hard state. The jet is steady, typically not very relativistic, and may extend up to a few tens of AU. *Transient jets* are instead observed when a source switches from the hard to the soft state and crosses the “jet line” (see Fig. 9). These pc-scale jets appear as blobs of plasma emitting mainly in the radio band and are relativistic. They have features similar to the kpc-scale jets observed in AGN and for this reason the black hole binaries producing transient jets are also called microquasars [95].

If the mechanism responsible for the formation of jets were the Blandford-Znajek model, one may expect a correlation between black hole spin measurements and estimates of the jet power. The authors of Ref. [37] have studied spin measurements of black hole binaries reported in the literature and inferred from the continuum-fitting and the iron line methods. Their plots do not show any correlation between black hole spin and jet power. The authors of Ref. [99] have proposed that the Blandford-Znajek mechanism is responsible for the formation of transient jets. They selected some spin measurements obtained via the continuum-fitting method and used a different proxy for the jet power. They find a correlation between black hole spin measurements and jet power. For the moment, this is a controversial issue [125, 86]. Both conclusions are based on a small number of data with large uncertainty. Future observations should be able to increase the number of sources and decrease the uncertainty in these measurements, and provide a conclusive answer to this issue [86].

### 8.2.2 Supermassive black holes

In the case of AGN, only a small fraction of them, around 1%, exhibit relativistic kpc-scale jets. One of the most spectacular examples is Cygnus A, see Fig. 18. Radio images of this object show two very collimated jets from the very center of the galaxy, where it is supposed to be located its supermassive black hole. The two jets extend well outside the galaxy, for hundreds of kpc.

Jets dominate the spectrum of a source at radio frequencies. There are apparently two distinct populations of AGN (see Fig. 10): radio-loud AGN and radio-quiet AGN [131]. This is particularly evident on the plane optical luminosity vs radio luminosity. For the same optical luminosity, radio-loud AGN have a radio luminosity 3-4 orders of magnitude higher than that of radio-quiet AGN. These two populations seem really to follow two different tracks with a gap between them.

The origin of the radio-quiet/radio-loud dichotomy is not understood [131]. Some authors have also doubted about the actual existence of this dichotomy, suggesting it is a bias of observations.

In the case of AGN with an accretion luminosity above 1% of the Eddington limit, the most natural interpretation is that their jets are the counterpart of the tran-

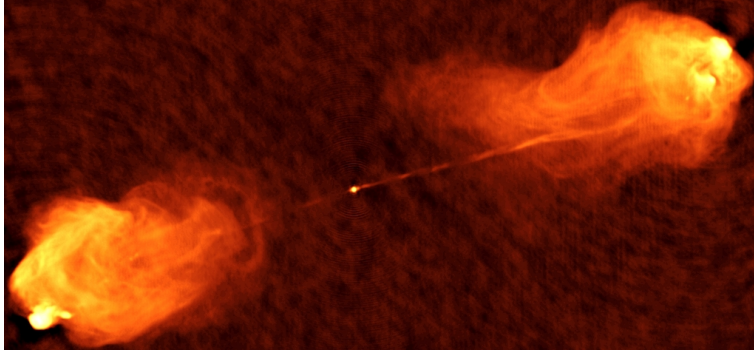


Fig. 18: Radio image of Cygnus A. The bright dot at the center is the location of the supermassive black hole, where the two relativistic jets are generated. The jets are stopped by the intergalactic medium, forming two giant lobes. Image courtesy of NRAO/AUI.

sient jets in black hole binaries. This conclusion may be supported by the consideration that microquasars show intermittent jets for a few percent of the time, which is similar to the fraction of radio-loud AGN [103]. The time scale of these systems is proportional to their mass, so intermittent jets in black hole binaries look like persistent jets in AGN. However, in the case of AGN with a luminosity below 1% of the Eddington limit, this explanation cannot work: black hole binaries with a low accretion luminosity are all radio-loud.

Another popular interpretation is that the dichotomy is determined by the black hole spin. When the accretion luminosity is low, it turns out that radio-loud AGN are in elliptical galaxies, while radio-quiet AGN are mainly in spiral galaxies. Galaxies with different morphology have likely a different merger and accretion history. This, in turn, may have produced two populations of black holes, with high and low values of spin [157]. A difference in radio luminosity of 3-4 orders of magnitude between the two populations is impossible to explain if the jet power is proportional to  $\Omega_{\text{H}}^2$ , but in the case of thick disks the jet power may scale as  $\Omega_{\text{H}}^6$  [145].

If jets are powered by the rotational energy of the accreting compact object, it is possible to extract energy and have an accretion efficiency  $\eta > 1$ . Some observations indicate that some AGN may have  $\eta > 1$  [50, 89]. If these measurements are correct, the jet is extracting energy from the system, and it is likely that this is the rotational energy of the black hole; some version of the Blandford-Znajek mechanism is working. While in the past some general-relativistic magnetohydrodynamic simulations have not been able to find high efficiency from the formation of jets, more recently simulations in which  $\eta > 1$  have been presented in Ref. [146].

## References

1. B. P. Abbott *et al.* [LIGO Scientific and Virgo Collaborations], *Phys. Rev. Lett.* **116**, 061102 (2016) [arXiv:1602.03837 [gr-qc]].
2. M. A. Abramowicz, M. Calvani and L. Nobili, *Astrophys. J.* **242**, 772 (1980).
3. M. A. Abramowicz, B. Czerny, J. P. Lasota and E. Szuszkiewicz, *Astrophys. J.* **332**, 646 (1988).
4. M. A. Abramowicz and P. C. Fragile, *Living Rev. Rel.* **16**, 1 (2013) [arXiv:1104.5499 [astro-ph.HE]].
5. M. A. Abramowicz and W. Kluzniak, *Astron. Astrophys.* **374**, L19 (2001) [astro-ph/0105077].
6. M. A. Abramowicz, W. Kluzniak, Z. Stuchlik and G. Torok, *Astron. Astrophys.* **436**, 1 (2005) [astro-ph/0401464].
7. M. A. Abramowicz and J. P. Lasota, *Acta Astron.* **30**, 35 (1980).
8. E. Agol, M. Kamionkowski, L. V. E. Koopmans and R. D. Blandford, *Astrophys. J.* **576**, L131 (2002) [astro-ph/0203257].
9. M. Bachetti *et al.*, *Nature* **514**, 202 [arXiv:1410.3590 [astro-ph.HE]].
10. C. Bambi, *Black Holes: A Laboratory for Testing Strong Gravity* (Springer Singapore, 2017), doi:10.1007/978-981-10-4524-0
11. J. M. Bardeen, *Timelike and null geodesics in the Kerr metric* in “Black Holes”, ed. C. DeWitt & B. S. DeWitt, (Gordon & Breach, 1973), pp. 215-239.
12. J. M. Bardeen and J. A. Petterson, *Astrophys. J.* **195**, L65 (1975).
13. J. E. Barnes and L. Hernquist, *Astrophys. J.* **471**, 115 (1996).
14. K. Belczynski, T. Bulik, C. L. Fryer, A. Rüter, J. S. Vink and J. R. Hurley, *Astrophys. J.* **714**, 1217 (2010) [arXiv:0904.2784 [astro-ph.SR]].
15. T. M. Belloni, *Lect. Notes Phys.* **794**, 53 (2010) [arXiv:0909.2474 [astro-ph.HE]].
16. E. Berti and M. Volonteri, *Astrophys. J.* **684**, 822 (2008) [arXiv:0802.0025 [astro-ph]].
17. R. D. Blandford and D. G. Payne, *Mon. Not. Roy. Astron. Soc.* **199**, 883 (1982).
18. R. D. Blandford and R. L. Znajek, *Mon. Not. Roy. Astron. Soc.* **179**, 433 (1977).
19. H. Bondi, *Mon. Not. Roy. Astron. Soc.* **112**, 195 (1952).
20. L. Brenneman, *Measuring Supermassive Black Hole Spins in Active Galactic Nuclei* (Springer New York, 2013) [arXiv:1309.6334 [astro-ph.HE]].
21. L. W. Brenneman and C. S. Reynolds, *Astrophys. J.* **652**, 1028 (2006) [astro-ph/0608502].
22. L. W. Brenneman, G. Risaliti, M. Elvis and E. Nardini, *Mon. Not. Roy. Astron. Soc.* **429**, 2662 (2013) [arXiv:1212.0772 [astro-ph.HE]].
23. L. W. Brenneman *et al.*, *Astrophys. J.* **736**, 103 (2011) [arXiv:1104.1172 [astro-ph.HE]].
24. J. Casares and P. G. Jonker, *Space Sci. Rev.* **183**, 223 (2014) [arXiv:1311.5118 [astro-ph.HE]].
25. Z. Chen, L. Gou, J. E. McClintock, J. F. Steiner, J. Wu, W. Xu, J. Orosz and Y. Xiang, arXiv:1601.00615 [astro-ph.HE].
26. C. Y. Chiang, R. C. Reis, D. J. Walton and A. C. Fabian, *Mon. Not. Roy. Astron. Soc.* **425**, 2436 (2012) [arXiv:1207.0682 [astro-ph.HE]].
27. E. J. M. Colbert and R. F. Mushotzky, *Astrophys. J.* **519**, 89 (1999) [astro-ph/9901023].
28. M. Coleman Miller and E. J. M. Colbert, *Int. J. Mod. Phys. D* **13**, 1 (2004) [arXiv:astro-ph/0308402].
29. T. Dauser, J. Garcia, J. Wilms, M. Bock, L. W. Brenneman, M. Falanga, K. Fukumura and C. S. Reynolds, *Mon. Not. Roy. Astron. Soc.* **430**, 1694 (2013) [arXiv:1301.4922 [astro-ph.HE]].
30. A. M. El-Batal *et al.*, *Astrophys. J.* **826**, L12 (2016) [arXiv:1607.00343 [astro-ph.HE]].
31. A. C. Fabian, K. Iwasawa, C. S. Reynolds and A. J. Young, *Publ. Astron. Soc. Pac.* **112**, 1145 (2000) [astro-ph/0004366].
32. A. C. Fabian, A. Lohfink, E. Kara, M. L. Parker, R. Vasudevan and C. S. Reynolds, *Mon. Not. Roy. Astron. Soc.* **451**, 4375 (2015) [arXiv:1505.07603 [astro-ph.HE]].
33. A. C. Fabian *et al.*, *Mon. Not. Roy. Astron. Soc.* **424**, 217 (2012) [arXiv:1204.5854 [astro-ph.HE]].
34. H. Falcke, F. Melia and E. Agol, *Astrophys. J.* **528**, L13 (2000) [astro-ph/9912263].

35. W. M. Farr, N. Sravan, A. Cantrell, L. Kreidberg, C. D. Bailyn, I. Mandel and V. Kalogera, *Astrophys. J.* **741**, 103 (2011) [arXiv:1011.1459 [astro-ph.GA]].
36. R. P. Fender, T. M. Belloni and E. Gallo, *Mon. Not. Roy. Astron. Soc.* **355**, 1105 (2004) [astro-ph/0409360].
37. R. Fender, E. Gallo and D. Russell, *Mon. Not. Roy. Astron. Soc.* **406**, 1425 (2010) [arXiv:1003.5516 [astro-ph.HE]].
38. L. Ferrarese *et al.*, *Astrophys. J.* **644**, L21 (2006) [astro-ph/0603840].
39. P. C. Fragile, O. M. Blaes, P. Annino and J. D. Salmonson, *Astrophys. J.* **668**, 417 (2007) [arXiv:0706.4303 [astro-ph]].
40. T. Fragos, M. Tremmel, E. Rantsiou and K. Belczynski, *Astrophys. J.* **719**, L79 (2010) [arXiv:1001.1107 [astro-ph.HE]].
41. T. Fragos and J. E. McClintock, *Astrophys. J.* **800**, 17 (2015) [arXiv:1408.2661 [astro-ph.HE]].
42. L. C. Gallo, G. Miniutti, J. M. Miller, L. W. Brenneman, A. C. Fabian, M. Guainazzi and C. S. Reynolds, *Mon. Not. Roy. Astron. Soc.* **411**, 607 (2011) [arXiv:1009.2987 [astro-ph.HE]].
43. E. Gallo, T. Treu, J. Jacob, J. H. Woo, P. Marshall and R. Antonucci, *Astrophys. J.* **680**, 154 (2008) [arXiv:0711.2073 [astro-ph]].
44. J. Garcia, T. Dauser, C. S. Reynolds, T. R. Kallman, J. E. McClintock, J. Wilms and W. Eikmann, *Astrophys. J.* **768**, 146 (2013) [arXiv:1303.2112 [astro-ph.HE]].
45. J. Garcia *et al.*, *Astrophys. J.* **813**, 84 (2015) [arXiv:1505.03607 [astro-ph.HE]].
46. J. A. Garcia *et al.*, *Astrophys. J.* **864**, 25 (2018) [arXiv:1807.01949 [astro-ph.HE]].
47. K. Gebhardt, R. M. Rich and L. C. Ho, *Astrophys. J.* **578**, L41 (2002) [astro-ph/0209313].
48. K. Gebhardt, R. M. Rich and L. C. Ho, *Astrophys. J.* **634**, 1093 (2005) [astro-ph/0508251].
49. A. M. Ghez, S. Salim, S. D. Hornstein, A. Tanner, M. Morris, E. E. Becklin and G. Duchene, *Astrophys. J.* **620**, 744 (2005) [astro-ph/0306130].
50. G. Ghisellini, F. Tavecchio, L. Foschini, G. Ghirlanda, L. Maraschi and A. Celotti, *Mon. Not. Roy. Astron. Soc.* **402**, 497 (2010) [arXiv:0909.0932 [astro-ph.CO]].
51. M. Gierlinski, M. Middleton, M. Ward and C. Done, *Nature* **455**, 369 (2008) [arXiv:0807.1899 [astro-ph]].
52. L. Gou, J. E. McClintock, J. Liu, R. Narayan, J. F. Steiner, R. A. Remillard, J. A. Orosz and S. W. Davis, *Astrophys. J.* **701**, 1076 (2009) [arXiv:0901.0920 [astro-ph.HE]].
53. L. Gou, J. E. McClintock, J. F. Steiner, R. Narayan, A. G. Cantrell, C. D. Bailyn and J. A. Orosz, *Astrophys. J.* **718**, L122 (2010) [arXiv:1002.2211 [astro-ph.HE]].
54. L. Gou *et al.*, *Astrophys. J.* **742**, 85 (2011) [arXiv:1106.3690 [astro-ph.HE]].
55. L. Gou *et al.*, *Astrophys. J.* **790**, 29 (2014) [arXiv:1308.4760 [astro-ph.HE]].
56. F. Haardt and L. Maraschi, *Astrophys. J.* **380**, L51 (1991).
57. F. Haardt and L. Maraschi, *Astrophys. J.* **413**, 507 (1993).
58. A. Heger, C. L. Fryer, S. E. Woosley, N. Langer and D. H. Hartmann, *Astrophys. J.* **591**, 288 (2003) [astro-ph/0212469].
59. A. Heger and S. E. Woosley, *Astrophys. J.* **567**, 532 (2002) [astro-ph/0107037].
60. J. Homan and T. Belloni, *Astrophys. Space Sci.* **300**, 107 (2005) [astro-ph/0412597].
61. S. A. Hughes and R. D. Blandford, *Astrophys. J.* **585**, L101 (2003) [astro-ph/0208484].
62. A. Ingram, C. Done and P. C. Fragile, *Mon. Not. Roy. Astron. Soc.* **397**, L101 (2009).
63. M. Jaroszynski, M. A. Abramowicz and B. Paczynski, *Acta Astron.* **30**, 1 (1980).
64. V. Kalogera and G. Baym, *Astrophys. J.* **470**, L61 (1996).
65. P. D. Kiel and J. R. Hurley, *Mon. Not. Roy. Astron. Soc.* **369**, 1152 (2006) [astro-ph/0605080].
66. A. R. King and U. Kolb, *Mon. Not. Roy. Astron. Soc.* **305**, 654 (1999) [astro-ph/9901296].
67. A. R. King, S. H. Lubow, G. I. Ogilvie and J. E. Pringle, *Mon. Not. Roy. Astron. Soc.* **363**, 49 (2005) [astro-ph/0507098].
68. A. R. King and J. E. Pringle, *Mon. Not. Roy. Astron. Soc.* **373**, L93 (2006) [astro-ph/0609598].
69. M. Y. Khlopov, *Res. Astron. Astrophys.* **10**, 495 (2010) [arXiv:0801.0116 [astro-ph]].
70. M. Kolehmainen and C. Done, *Mon. Not. Roy. Astron. Soc.* **406**, 2206 (2010) [arXiv:0911.3281 [astro-ph.HE]].

71. J. Kormendy and D. Richstone, *Ann. Rev. Astron. Astrophys.* **33**, 581 (1995).
72. A. K. Kulkarni *et al.*, *Mon. Not. Roy. Astron. Soc.* **414**, 1183 (2011) [arXiv:1102.0010 [astro-ph.HE]].
73. S. Kumar and J. E. Pringle, *Mon. Not. Roy. Astron. Soc.* **213**, 435 (1985).
74. J. P. Lasota, *Black hole accretion discs*, doi:10.1007/978-3-662-52859-4\_1 arXiv:1505.02172 [astro-ph.HE].
75. J. M. Lattimer, *Ann. Rev. Nucl. Part. Sci.* **62**, 485 (2012) [arXiv:1305.3510 [nucl-th]].
76. L. X. Li, E. R. Zimmerman, R. Narayan and J. E. McClintock, *Astrophys. J. Suppl.* **157**, 335 (2005) [astro-ph/0411583].
77. J. Liu, J. McClintock, R. Narayan, S. Davis and J. Orosz, *Astrophys. J.* **679**, L37 (2008) [Erratum: *Astrophys. J.* **719**, L109 (2010)] [arXiv:0803.1834 [astro-ph]].
78. G. Lodato and J. E. Pringle, *Mon. Not. Roy. Astron. Soc.* **368**, 1196 (2006) [astro-ph/0602306].
79. A. M. Lohfink *et al.*, *Astrophys. J.* **772**, 83 (2013) [arXiv:1305.4937 [astro-ph.HE]].
80. P. Madau, F. Haardt and M. Dotti, *Astrophys. J.* **784**, L38 (2014) [arXiv:1402.6995 [astro-ph.CO]].
81. E. Maoz, *Astrophys. J.* **494**, L181 (1998) [astro-ph/9710309].
82. A. Marinucci *et al.*, *Astrophys. J.* **787**, 83 (2014) [arXiv:1404.3561 [astro-ph.HE]].
83. R. G. Martin, J. E. Pringle and C. A. Tout, *Mon. Not. Roy. Astron. Soc.* **381**, 1617 (2007) [arXiv:0708.2034 [astro-ph]].
84. R. G. Martin, C. A. Tout and J. E. Pringle, *Mon. Not. Roy. Astron. Soc.* **387**, 188 (2008) [arXiv:0802.3912 [astro-ph]].
85. L. Mayer, S. Kazantzidis, P. Madau, M. Colpi, T. R. Quinn and J. Wadsley, *Science* **316**, 1874 (2007) [arXiv:0706.1562 [astro-ph]].
86. J. E. McClintock, R. Narayan and J. F. Steiner, *Space Sci. Rev.* **183**, 295 (2014) [arXiv:1303.1583 [astro-ph.HE]].
87. J. E. McClintock, R. Shafee, R. Narayan, R. A. Remillard, S. W. Davis and L. X. Li, *Astrophys. J.* **652**, 518 (2006) [astro-ph/0606076].
88. J. E. McClintock *et al.*, *Class. Quant. Grav.* **28**, 114009 (2011) [arXiv:1101.0811 [astro-ph.HE]].
89. B. R. McNamara, M. Rohanizadegan and P. E. J. Nulsen, *Astrophys. J.* **727**, 39 (2011) [arXiv:1007.1227 [astro-ph.CO]].
90. D. L. Meier, *Astrophys. J.* **548**, L9 (2001) [astro-ph/0010231].
91. M. Middleton, J. Miller-Jones and R. Fender, *Mon. Not. Roy. Astron. Soc.* **439**, 1740 (2014) [arXiv:1401.1829 [astro-ph.HE]].
92. J. M. Miller *et al.*, *Astrophys. J.* **775**, L45 (2013) [arXiv:1308.4669 [astro-ph.HE]].
93. J. M. Miller *et al.*, *Astrophys. J.* **860**, L28 (2018) [arXiv:1806.04115 [astro-ph.HE]].
94. G. Miniutti, F. Panessa, A. De Rosa, A. C. Fabian, A. Malizia, M. Molina, J. M. Miller and S. Vaughan, *Mon. Not. Roy. Astron. Soc.* **398**, 255 (2009) [arXiv:0905.2891 [astro-ph.HE]].
95. I. F. Mirabel and L. F. Rodriguez, *Ann. Rev. Astron. Astrophys.* **37**, 409 (1999) [astro-ph/9902062].
96. K. Mitsuda *et al.*, *Publ. Astron. Soc. Jap.* **36**, 741 (1984).
97. S. E. Motta, T. M. Belloni, L. Stella, T. Muñoz-Darias and R. Fender, *Mon. Not. Roy. Astron. Soc.* **437**, 2554 (2014) [arXiv:1309.3652 [astro-ph.HE]].
98. S. E. Motta, T. Muñoz-Darias, A. Sanna, R. Fender, T. Belloni and L. Stella, *Mon. Not. Roy. Astron. Soc.* **439**, 65 (2014) [arXiv:1312.3114 [astro-ph.HE]].
99. R. Narayan and J. E. McClintock, *Mon. Not. Roy. Astron. Soc.* **419**, L69 (2012) [arXiv:1112.0569 [astro-ph.HE]].
100. R. Narayan and I. Yi, *Astrophys. J.* **428**, L13 (1994) [astro-ph/9403052].
101. R. Narayan and I. Yi, *Astrophys. J.* **452**, 710 (1995) [astro-ph/9411059].
102. E. Nardini, A. C. Fabian, R. C. Reis and D. J. Walton, *Mon. Not. Roy. Astron. Soc.* **410**, 1251 (2011) [arXiv:1008.2157 [astro-ph.HE]].
103. C. Nipoti, K. M. Blundell and J. Binney, *Mon. Not. Roy. Astron. Soc.* **361**, 633 (2005) [astro-ph/0505280].



104. I. D. Novikov and K. S. Thorne, *Astrophysics and black holes*, in *Black Holes*, edited by C. De Witt and B. De Witt (Gordon and Breach, New York, New York, 1973).
105. K. Ohsuga and S. Mineshige, *Astrophys. J.* **736**, 2 (2011) [arXiv:1105.5474 [astro-ph.HE]].
106. D. N. Page and K. S. Thorne, *Astrophys. J.* **191**, 499 (1974).
107. M. L. Parker *et al.*, *Mon. Not. Roy. Astron. Soc.* **443**, no. 2, 1723 (2014) [arXiv:1407.8223 [astro-ph.HE]].
108. M. L. Parker *et al.*, *Astrophys. J.* **808**, 9 (2015) [arXiv:1506.00007 [astro-ph.HE]].
109. M. L. Parker *et al.*, *Astrophys. J.* **821**, L6 (2016) [arXiv:1603.03777 [astro-ph.HE]].
110. D. R. Pasham, T. E. Strohmayer and R. F. Mushotzky, *Nature* **513**, 74 (2014) [arXiv:1501.03180 [astro-ph.HE]].
111. A. R. Patrick, J. N. Reeves, D. Porquet, A. G. Markowitz, V. Braito and A. P. Lobban, *Mon. Not. Roy. Astron. Soc.* **426**, 2522 (2012) [arXiv:1208.1150 [astro-ph.HE]].
112. R. F. Penna, J. C. McKinney, R. Narayan, A. Tchekhovskoy, R. Shafee and J. E. McClintock, *Mon. Not. Roy. Astron. Soc.* **408**, 752 (2010) [arXiv:1003.0966 [astro-ph.HE]].
113. R. Penrose, *Riv. Nuovo Cim.* **1**, 252 (1969) [*Gen. Rel. Grav.* **34**, 1141 (2002)].
114. M. Postman *et al.*, *Astrophys. J.* **756**, 159 (2012) [arXiv:1205.3839 [astro-ph.CO]].
115. M. J. Reid, J. E. McClintock, J. F. Steiner, D. Steeghs, R. A. Remillard, V. Dhawan and R. Narayan, *Astrophys. J.* **796**, 2 (2014) [arXiv:1409.2453 [astro-ph.GA]].
116. R. C. Reis, A. C. Fabian, R. R. Ross and J. M. Miller, *Mon. Not. Roy. Astron. Soc.* **395**, 1257 (2009).
117. R. C. Reis, A. C. Fabian, R. Ross, G. Miniutti, J. M. Miller and C. Reynolds, *Mon. Not. Roy. Astron. Soc.* **387**, 1489 (2008) [arXiv:0804.0238 [astro-ph]].
118. R. C. Reis and J. M. Miller, *Astrophys. J.* **769**, L7 (2013) [arXiv:1304.4947 [astro-ph.HE]].
119. R. C. Reis, J. M. Miller, M. T. Reynolds, A. C. Fabian and D. J. Walton, *Astrophys. J.* **751**, 34 (2012) [arXiv:1111.6665 [astro-ph.HE]].
120. R. C. Reis *et al.*, *Mon. Not. Roy. Astron. Soc.* **410**, 2497 (2011) [arXiv:1009.1154 [astro-ph.HE]].
121. R. A. Remillard and J. E. McClintock, *Ann. Rev. Astron. Astrophys.* **44**, 49 (2006) [astro-ph/0606352].
122. C. S. Reynolds, *Space Sci. Rev.* **183**, 277 (2014) [arXiv:1302.3260 [astro-ph.HE]].
123. C. E. Rhoades and R. Ruffini, *Phys. Rev. Lett.* **32**, 324 (1974).
124. G. Risaliti *et al.*, *Nature* **494**, 449 (2013) [arXiv:1302.7002 [astro-ph.HE]].
125. D. M. Russell, E. Gallo and R. P. Fender, *Mon. Not. Roy. Astron. Soc.* **431**, 405 (2013) [arXiv:1301.6771 [astro-ph.HE]].
126. S. Schmoll *et al.*, *Astrophys. J.* **703**, 2171 (2009) [arXiv:0908.0013 [astro-ph.HE]].
127. R. Shafee, J. E. McClintock, R. Narayan, S. W. Davis, L. X. Li and R. A. Remillard, *Astrophys. J.* **636**, L113 (2006) [astro-ph/0508302].
128. N. I. Shakura and R. A. Sunyaev, *Astron. Astrophys.* **24**, 337 (1973).
129. S. L. Shapiro and S. A. Teukolsky, *Black holes, white dwarfs, and neutron stars: The physics of compact objects* (Wiley-VCH, 1983).
130. I. Shlosman, M. C. Begelman and J. Frank, *Nature* **345**, 679 (1990).
131. M. Sikora, L. Stawarz and J. P. Lasota, *Astrophys. J.* **658**, 815 (2007) [astro-ph/0604095].
132. M. Spera, M. Mapelli and A. Bressan, *Mon. Not. Roy. Astron. Soc.* **451**, no. 4, 4086 (2015) [arXiv:1505.05201 [astro-ph.SR]].
133. J. F. Steiner and J. E. McClintock, *Astrophys. J.* **745**, 136 (2012) [arXiv:1110.6849 [astro-ph.HE]].
134. J. F. Steiner, J. E. McClintock, J. A. Orosz, R. A. Remillard, C. D. Bailyn, M. Kolehmainen and O. Straub, *Astrophys. J.* **793**, L29 (2014) [arXiv:1402.0148 [astro-ph.HE]].
135. J. F. Steiner, J. E. McClintock, R. A. Remillard, L. Gou, S. Yamada and R. Narayan, *Astrophys. J.* **718**, L117 (2010) [arXiv:1006.5729 [astro-ph.HE]].
136. J. F. Steiner, J. E. McClintock and M. J. Reid, *Astrophys. J.* **745**, L7 (2012) [arXiv:1111.2388 [astro-ph.HE]].
137. J. F. Steiner, D. J. Walton, J. A. Garcia, J. E. McClintock, S. G. T. Laycock, M. J. Middleton, R. Barnard and K. K. Madsen, arXiv:1512.03414 [astro-ph.HE].

138. J. F. Steiner *et al.*, *Mon. Not. Roy. Astron. Soc.* **416**, 941 (2011) [arXiv:1010.1013 [astro-ph.HE]].
139. J. F. Steiner *et al.*, *Mon. Not. Roy. Astron. Soc.* **427**, 2552 (2012) [arXiv:1209.3269 [astro-ph.HE]].
140. L. Stella, M. Vietri and S. Morsink, *Astrophys. J.* **524**, L63 (1999) [astro-ph/9907346].
141. S. Sun, M. Guainazzi, Q. Ni, J. Wang, C. Qian, F. Shi, Y. Wang and C. Bambi, *Mon. Not. Roy. Astron. Soc.* **478**, 1900 (2018) [arXiv:1704.03716 [astro-ph.HE]].
142. R. A. Sunyaev and J. Truemper, *Nature* **279**, 506 (1979).
143. R. A. Sunyaev and L. G. Titarchuk, *Astron. Astrophys.* **86**, 121 (1980).
144. Y. Tan, J. Wang, X. Shu and Y. Zhou, *Astrophys. J.* **747**, L11 (2012) [arXiv:1202.0400 [astro-ph.HE]].
145. A. Tchekhovskoy, R. Narayan and J. C. McKinney, *Astrophys. J.* **711**, 50 (2010) [arXiv:0911.2228 [astro-ph.HE]].
146. A. Tchekhovskoy, R. Narayan and J. C. McKinney, *Mon. Not. Roy. Astron. Soc.* **418**, L79 (2011) [arXiv:1108.0412 [astro-ph.HE]].
147. K. S. Thorne, *Astrophys. J.* **191**, 507 (1974).
148. F. X. Timmes, S. E. Woosley and T. A. Weaver, *Astrophys. J.* **457**, 834 (1996) [astro-ph/9510136].
149. J. A. Tomsick *et al.*, *Astrophys. J.* **780**, 78 (2014) [arXiv:1310.3830 [astro-ph.HE]].
150. C. M. Urry and P. Padovani, *Publ. Astron. Soc. Pac.* **107**, 803 (1995) [astro-ph/9506063].
151. E. P. J. van den Heuvel, *Endpoints of stellar evolution: The incidence of stellar mass black holes in the galaxy*, in “Environment Observation and Climate Modelling Through International Space Projects”, 29 (1992).
152. M. van der Klis, astro-ph/0410551.
153. R. V. Vasudevan, A. C. Fabian, C. S. Reynolds, J. Aird, T. Dauser and L. C. Gallo, *Mon. Not. Roy. Astron. Soc.* **458**, 2012 (2016) [arXiv:1506.01027 [astro-ph.HE]].
154. M. Volonteri, *Astron. Astrophys. Rev.* **18**, 279 (2010) [arXiv:1003.4404 [astro-ph.CO]].
155. M. Volonteri, F. Haardt and K. Gultekin, *Mon. Not. Roy. Astron. Soc.* **384**, 1387 (2008) [arXiv:0710.5770 [astro-ph]].
156. M. Volonteri, G. Lodato and P. Natarajan, *Mon. Not. Roy. Astron. Soc.* **383**, 1079 (2008) [arXiv:0709.0529 [astro-ph]].
157. M. Volonteri, M. Sikora and J. P. Lasota, *Astrophys. J.* **667**, 704 (2007) [arXiv:0706.3900 [astro-ph]].
158. D. J. Walton, R. C. Reis, E. M. Cackett, A. C. Fabian and J. M. Miller, *Mon. Not. Roy. Astron. Soc.* **422**, 2510 (2012) [arXiv:1202.5193 [astro-ph.HE]].
159. D. J. Walton, E. Nardini, A. C. Fabian, L. C. Gallo and R. C. Reis, *Mon. Not. Roy. Astron. Soc.* **428**, 2901 (2013) [arXiv:1210.4593 [astro-ph.HE]].
160. D. J. Walton *et al.*, *Astrophys. J.* **826**, 87 (2016) [arXiv:1605.03966 [astro-ph.HE]].
161. J. M. Wang, Y. M. Chen, L. C. Ho and R. J. McLure, *Astrophys. J.* **642**, L111 (2006) [astro-ph/0603813].
162. N. White, *Nature* **407**, 146 (2000).
163. S. E. Woosley and J. S. Bloom, *Ann. Rev. Astron. Astrophys.* **44**, 507 (2006) [astro-ph/0609142].
164. X.-B. Wu *et al.*, *Nature* **518**, 512 (2015).
165. Y. Xu *et al.*, *Astrophys. J.* **852**, L34 (2018) [arXiv:1711.01346 [astro-ph.HE]].
166. Y. Xu *et al.*, arXiv:1805.07705 [astro-ph.HE].
167. S. C. Yoon, N. Langer and C. Norman, *Astron. Astrophys.* **460**, 199 (2006) [astro-ph/0606637].
168. L. R. Yungelson, J.-P. Lasota, G. Nelemans, G. Dubus, E. P. J. van den Heuvel, J. Dewi and S. Portegies Zwart, *Astron. Astrophys.* **454**, 559 (2006) [astro-ph/0604434].
169. J. A. Zensus, *Ann. Rev. Astron. Astrophys.* **35**, 607 (1997).
170. S. N. Zhang, W. Cui and W. Chen, *Astrophys. J.* **482**, L155 (1997) [astro-ph/9704072].
171. V. V. Zhuravlev, P. B. Ivanov, P. C. Fragile and D. M. Teixeira, *Astrophys. J.* **796**, 104 (2014) [arXiv:1406.5515 [astro-ph.HE]].
172. A. Zoghbi, A. Fabian, P. Uttley, G. Miniutti, L. Gallo, C. Reynolds, J. Miller and G. Ponti, *Mon. Not. Roy. Astron. Soc.* **401**, 2419 (2010) [arXiv:0910.0367 [astro-ph.HE]].